Ocean Dynamics (2017) 67:321–343
DOI 10.1007/s10236-016-1026-z

Modeling of the Bosphorus exchange flow dynamics

Adil Sözer[1,2] · **Emin Özsoy**[1,3]

Received: 27 June 2016 / Accepted: 6 December 2016 / Published online: 25 January 2017

Abstract The fundamental hydrodynamic behavior of the Bosphorus Strait is investigated through a numerical modeling study using alternative configurations of idealized or realistic geometry. Strait geometry and basin stratification conditions allow for hydraulic controls and are ideally suited to support the maximal-exchange regime, which determines the rate of exchange of waters originating from the adjacent Black and Mediterranean Seas for a given net transport. Steady-state hydraulic controls are demonstrated by densimetric Froude number calculations under layered flow approximations when corrections are applied to account for high velocity shears typically observed in the Bosphorus. Analyses of the model results reveal many observed features of the strait, including critical transitions at hydraulic controls and dissipation by turbulence and hydraulic jumps. It is found that the solution depends on initialization, especially with respect to the basin initial conditions. Significant differences between the controlled maximal-exchange and drowned solutions suggest that a detailed modeling implementation involving coupling with adjacent basins needs to take full account of the Bosphorus Strait in terms of the physical processes to be resolved.

Keywords Bosphorus Strait · Hydraulic control · Exchange flow

Responsible Editor: Emil Vassilev Stanev

✉ Adil Sözer
adilsozer@gmail.com

[1] Institute of Marine Sciences, Middle East Technical University, Ankara, Turkey

[2] Present address: Fatsa Faculty of Marine Sciences, Ordu University, Ordu, Turkey

[3] Present address: Eurasia Institute of Earth Sciences, İstanbul Technical University, İstanbul, Turkey

1 Introduction

The Turkish Straits System (TSS) is a complex course of seawater formed by the Dardanelles and Bosphorus Straits and the Marmara Sea between them. This system controls the coupling and the interaction between the Black Sea and the Mediterranean Sea, two large basins of ultimate contrasts in water properties. The density difference and the consequent pressure gradient between the two adjacent basins were first noted by Marsigli (1681) as the main driving mechanism of the stratified exchange flows. The Bosphorus constitutes the main choke-point of this system as a result of the anticipated maximal-exchange regime (Farmer and Armi 1986), established by flow transitions over a sill near the Black Sea entrance and at a contraction in the southern part (Ünlüata et al. 1990; Latif et al. 1991).

Measurements have identified regions of interfacial instabilities, turbulence, and hydraulic transitions along the Bosphorus Strait and in the exit regions (Özsoy et al. 2001; Gregg and Özsoy 2002). Tidal oscillations in the region, typically of small amplitude (∼10 cm), do not have much potential to create mixing. Yet, Helmholtz and higher mode basin oscillations of few hours to few days and longer have been identified in the TSS (Filippi et al. 1986; Gregg and Özsoy 1999, 2002; Çetin 1999; Özsoy et al. 1998; Özsoy et al. 2009; Jarosz et al. 2011a, b). Occasional blocking of

the flows in either layer in response to mainly meteorologically forced transient events in the adjacent basins is a well-known part of the flow variability (Ünlüata et al. 1990; Latif et al. 1991; Özsoy et al. 1995, 1996, 1998, 2001; Özsoy and Ünlüata 1997, 1998; Jarosz et al. 2011a, b). To take on the grand challenge of constructing predictive models of the TSS has been largely set back because of the lack of sufficient understanding of its most restrictive element, the Bosphorus, later to be integrated within the complex realm of the TSS. Simplified models solving either horizontally or vertically integrated hydrodynamic equations have been developed for the Bosphorus (Oğuz et al. 1990; Ilıcak et al. 2009) and Dardanelles (Oğuz and Sur 1989; Stashchuk and Hutter 2001) Straits. Three-dimensional models solving the full set of primitive equations have later been developed for the Bosphorus Strait (Sözer and Özsoy 2002; Oğuz 2005; Sözer 2013).

We investigate the exchange flow dynamics of the Bosphorus Strait with an objective to understand and document its most elementary, steady-state response created by a net flux through the system. Our general objective is to investigate the basic behavior of the Bosphorus isolated from some of the more complicated effects imposed on it by both local and remote hydro-meteorological, oceanographic factors, in order to start to develop a basic physical understanding of its typically observed complicated response. The specific set of questions we try to answer in this regard are (i) whether hydraulic controls exist, and if so, where are their locations; (ii) if a maximal-exchange regime can be recovered from model results, as often suggested by observations and theoretical considerations; (iii) what is the structure of currents and what are the transports in each direction; (iv) how does the free surface vary along the strait and the exit regions, and what is the sea-level difference between the two ends as a function of net flux; (v) to which extent the counter-acting influences of turbulence generation and stable stratification react to varying conditions; (vi) whether the solutions are sensitive to certain types of initial and boundary conditions, or to numerical aspects such as the grid resolution, mixing schemes and parametrizations used; and (vii) are there major differences between the flow regime and predicted structure of an idealized configuration and those of the real Bosphorus, especially with regard to controlled flow? We utilize a sophisticated three-dimensional ocean model of sufficiently high resolution and with applied boundary conditions to test model response to such factors.

Although the systematic behavior of the TSS in response to transient changes in atmospheric pressure and wind, mass, and heat fluxes taking into account full coupling with adjacent basins warrants much detailed further investigations, we leave these subjects to be addressed by continuing studies.

The model description and setup are reviewed in Section 2. Then, the idealized model results are provided in Section 3, followed by realistic model results in Section 4. Conclusions are given in Section 5.

2 Model description and setup

We advance the efforts for Bosphorus Strait hydrodynamic modeling by making use of the ROMS, a well-documented and tested community model (Hedström 1997; Haidvogel et al. 2000; Shchepetkin and McWilliams 2005) allowing for a dynamic free surface, various mixing, higher-order advection, and turbulence closure schemes, with compatible boundary conditions. Two different model configurations are used for studying the steady exchange flows in the Bosphorus Strait: (i) a test case with idealized geometry for the analysis of model performance and sensitivity and (ii) a full configuration with accurate bottom topographic features and geometry to study the realistic behavior of the Bosphorus Strait.

The idealized model domain minimally representing key features of the Bosphorus is a rectangular channel of length 34 km and width 1300 m, with a symmetric contraction region of length 4 km and width of 700 m at the narrowest section located at about one-third of the strait from the southern end. The abrupt openings at the Marmara and the Black Sea ends are adjoined by reservoirs of 5100 m in width. A Gaussian shaped sill topography, 1 km in length and with a crest of 13 m above the bottom, is located at the junction of the channel with the northern reservoir. The bottom is otherwise flat with a constant depth of 70 m (Fig. 1). The model domain is discretized by a 55×512 rectilinear grid with $dx = dy = 100$ m and 35 vertical s-levels yielding variable vertical resolution of $dz = 1.6-2.0$ m.

In the idealized system, the lock-exchange (LE) initial condition is specified, in which water of differing salinity, with respective values of 38.0 and 19.0 are assumed to fill the southern and northern parts of the basin, meeting at mid-channel, as shown later in Fig. 5a. In this simple model, temperature is removed from the nonlinear equation of state, considering the greater contribution of salinity to the density difference between basins (amounting to 14.6 kg/m^3 in this case) driving the system.

Laplacian mixing along constant geopotential surfaces is assumed with eddy viscosity and diffusivity coefficients of $K_h = 15.0$ m^2/s in the horizontal and $K_v = 10^{-4}$ m^2/s in the vertical respectively, assumed to be equal for momentum and salt diffusion. The three-dimensional variables are subject to radiation boundary conditions at the open boundaries, while two-dimensional variables are assumed to satisfy the gradient boundary condition, except for the

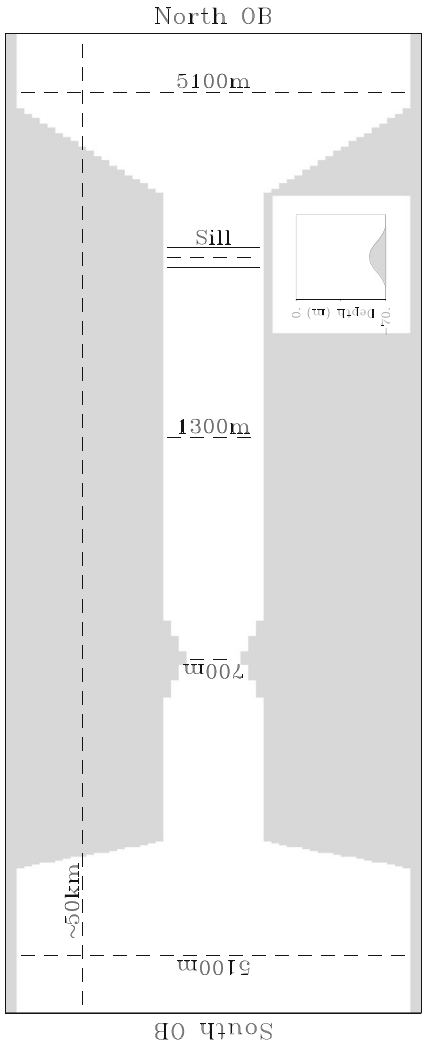

Fig. 1 Layout of the idealized model domain of the Bosphorus Strait. The domain is discretized on a 55 × 512 rectilinear grid with $dx = dy = 100$ m. Bottom is flat except for the sill region displayed in the inset

south-north component of the depth averaged velocity, ($\bar{v}$), specified at the south edge, with volume conservation additionally imposed at the two open boundaries. The specified southward barotropic current of $\bar{v} = -0.01$ m/s implies a southward net volume flux of ∼3500 m^3/s, corresponding to a moderate flow, as the mean annual net through-flow of the Bosphorus happens to be on the order of ∼10, 000 m^3/s (Ünlüata et al. 1990). No-slip boundary conditions are applied at the side-walls, and a quadratic bottom friction with a drag coefficient of 0.005 is specified at the bottom. Considering that the internal Rossby radius of deformation is significantly larger than the channel and the reservoir widths in the model, the rotation of the earth is ignored. To minimize over/under-shooting near the salinity front, the MPDATA scheme is selected for tracer advection while default schemes are utilized for 2d and 3d momentum.

The realistic model of Bosphorus Strait was configured on a rectilinear grid of 163 × 716 nodes with variable resolution of $dx = 50-200$ m, $dy = 50-325$ m and evenly spaced 35 s-levels resulting in $dz = 0.7-2.85$ m in the vertical. The bathymetry was largely derived from the high-resolution data of Gökaşan et al. (2005), complemented by additional data in adjacent basins, including those from the General Bathymetric Chart of the Oceans (www.gebco.net), as well as those formerly obtained by NRV Alliance of NATO Undersea Research Center (Di Iorio et al. 1999) and other digitized data from the maps of the Turkish Navy Office of Navigation, Hydrography and Oceanography used to fill the gaps. Minimal, scale-selective smoothing is applied to limit steepness in few areas and a minimum depth of 25 m is set in some shallow banks for concerns of numerical stability. Wider rectangular basins at the two extremities of the strait are included to represent the adjacent basins, while relaxation zones of uniform cross-section are allowed near the southern and northern boundaries (Fig. 2).

In the realistic geometry model, the generic length-scale (GLS) turbulence scheme, Warner et al. (2005), with the $k-\epsilon$ formulation was used with a background vertical mixing of $K_v = 10^{-5}$ m^2/s for all mixing variables. Lateral diffusivity and viscosity are parametrized by the Smagorinsky (1963) like formulation, applied on constant geopotential surfaces. In addition, radiation boundary conditions are applied for the 2d variables except for the depth averaged velocity ($\bar{v}$) prescribed at the southern boundary in order to impose a net volume flux through the strait. For the uniform reservoir solutions, 3d variables are radiated as in the case of the idealized system, while temperature and salinity are introduced at the boundaries for the stratified reservoir solutions, see Section 4.

3 Idealized model results

The idealized model is started from the lock-exchange (LE) initial condition and time-stepped with a baroclinic time-step of 3.5 s and a barotropic time-step of 0.175 s to ensure stable integration in the initial phase, followed by a restart with increased time-steps of 14 s and 0.7 s for a total duration of ∼4.1 days.

The final stratification that develops in the strait can be approximated as a two-layer system with relatively uniform properties in the layers, separated by a transition (interfacial) layer of thickness on the order of ∼10 m between them. The interface depth increases from south to north, with increased slopes near topographic barriers at the south-exit, the contraction, and the northern sill, anticipated to impose hydraulic transitions (Fig. 3a). A sea level difference of (∼0.4 m) is obtained between the reservoirs at the two ends of the strait, in accordance with the chosen net volume

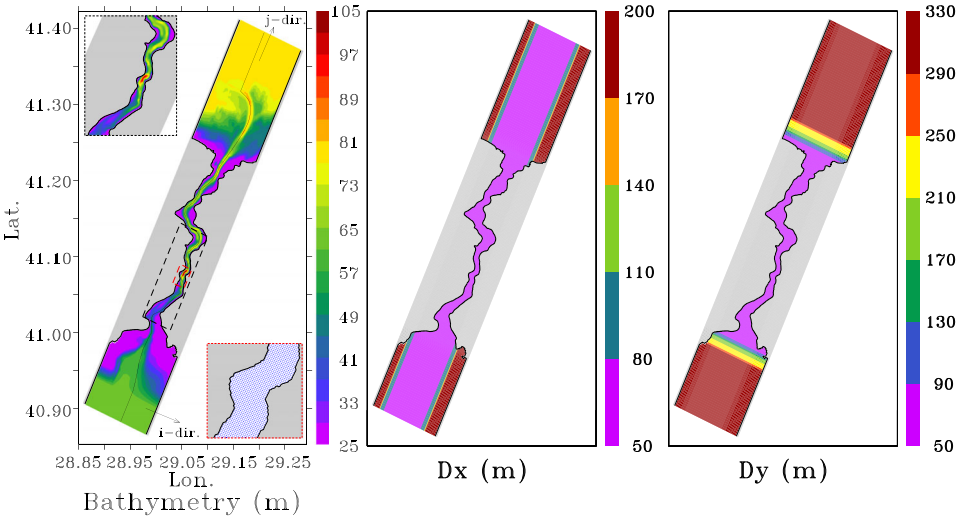

Fig. 2 (**a**) Layout and the bathymetry of the realistic model domain, with details of the bathymetry from south sill to the first bend (top-left) and demonstration of the grid nodes within the narrowest section of the strait (bottom-right). (**b**) The cross-channel and (**c**) along-channel grid size resolution of the rectilinear grid

flux. Close to the northern end of the strait, the free-surface varies linearly with distance, while rapid changes occur within the contraction zone and also the exit to the Marmara Sea (Fig. 3b). As demonstrated in Fig. 3b, the mid-section and laterally averaged sea-level responses are almost in perfect agreement through the channel, which is also confirmed to be valid for salinity. The only place where the lateral average differs slightly from the mid-section is at the southern exit where the surface flow separates from the coast and enters into the south reservoir (Marmara Sea) as a distinctive jet narrower than the channel width, with typical current speeds as high as 2 m/s, comparable in magnitude with lower-layer currents past the northern sill (on the Black Sea side).

An interesting result of the idealized model shown in Fig. 3a is the zero-velocity line being deeper than the salinity interface on the Marmara end and also shallower than the interface on the Black Sea end. This particular finding testifies to the general predictions of Tolmazin (1967, 1985) for stratified straits and reported by detailed measurements of Gregg and Özsoy (2002) in the Bosphorus Strait.

The model results show excellent conservation properties. A steady-state solution is achieved few days after initialization with perfect mass and energy conservation properties. Some limited over/under-shooting behavior was observed in the salinity field especially within the sill region where sharp gradients exist in the vertical and horizontal directions. We also find that the model rather realistically reproduces some basic characteristics of the Bosphorus.

3.1 Hydraulic controls

Although the maximal-exchange theory of Farmer and Armi (1986) presents an elegant and simple solution for the

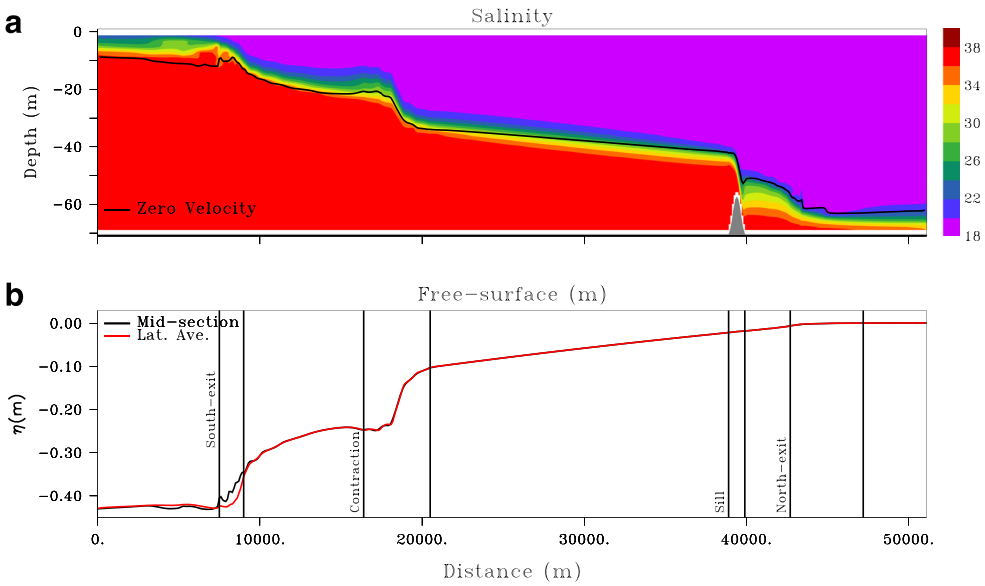

Fig. 3 Steady-state (day ∼4.1) along-channel variations of laterally-averaged salinity (*color*) and the zero-velocity isotach (*solid black line*) (**a**), mid-channel (*black line*) and laterally averaged (*red*) free-surface elevation (**b**) for the ideal case solution started from the lock-exchange initial condition with a net barotropic flux of ∼3500 m^3/s

specific type of strait flow for which the Bosphorus Strait appears to be the prime example, the demonstration of its existence, based on either measurements or model results, is not simple. The analysis often depends on the definition of layers not directly applicable to continuously stratified flow over complex topography. In the case of Gibraltar Strait, hydraulic control could only be shown during certain phases of the tidal cycle, differing significantly for the types of models used (Sannino et al. 2009). Measurements, even those with elaborate experimental design, appeared often inconclusive to demonstrate hydraulic controls, such as at the Bab-el Mandab Strait (Pratt et al. 1999).

For a gradually varying two-layer flow with inviscid homogenous fluid in each layer, the composite densimetric Froude-number is used to characterize the flow:

$$G^2 = F_1^2 + F_2^2 - \epsilon F_1^2 F_2^2, \quad (1)$$

where

$$F_i^2 = \frac{u_i^2}{g' y_i}; \quad i = 1, 2 \quad (2)$$

are the internal Froude-numbers of the individual layers, and u_i and y_i respectively are the velocity and the thickness of the layers. Here, $g' = g\epsilon = g\Delta\rho/\rho$ is the reduced gravity, and the ratio $\epsilon \equiv \Delta\rho/\rho_2 = (\rho_2 - \rho_1)/\rho_2$ (Armi 1986) is typically a small number, on the order of 10^{-2} or less in the case of the Bosphorus; therefore, the last term of (1) is negligible. Hydraulic control is identified when the composite densimetric Froude-number passes through the critical value $G^2 = 1$ at the hydraulic transition, and the flow becomes supercritical ($G^2 > 1$).

The composite densimetric Froude-number is used to investigate the existence of hydraulic controls in the Bosphorus, based on the definition of layers either by using the zero-velocity surface separating currents in opposite directions or the salinity interface approximated as the average of depths where 10 % change in salinity occurs relative to the surface and bottom values. Alternatively, a layer separation stream surface can be identified between the uppermost northward flowing stream-surface originating from the south of the sill reaching the contraction and similarly, finding the lowest southward flowing stream-surface originating from the north of the contraction and reaching the sill.

The variation of the two-layer composite densimetric Froude-number G^2 with distance along the strait is demonstrated in Fig. 4a under the assumption of vertically constant width for each layer, for three alternative definitions based on velocity, salinity, and the stream-surface. The component F_1^2 dominates the composite Froude-number when an active upper-layer flows through the contraction and the southern exit (not shown), while F_2^2 is the dominant component over the sill.

As pointed out by Garrett and Gerdes (2003) and Pratt (2008), the simple two-layer approximation for the composite densimetric Froude-number often underestimates the expected value in the presence of shear, because of average values of layer velocity and thickness being used in the computation. For flows having sluggish parts relative to a faster moving core, both the horizontal and the vertical integration of the quadratic term in velocity would evidently yield smaller values of the Froude-number. In the case of a single layer with vertical shear, Garrett and Gerdes (2003) proposed to correct the Froude-number calculated from the mean values with a dimensionless momentum flux factor $M = \int P^2(\zeta) d\zeta$ originating from integration with respect to the coordinate $\zeta = z/h$ spanning the shear profile over depth h, where $P(\zeta)$ is the dimensionless shape function for the velocity profile normalized such that $\int P(\zeta) d\zeta = 1$. An analogous energy flux factor $E = \int P^3(\zeta) d\zeta$ occurs in the corresponding energy flux terms. Both of these factors are less than unity by definition, following from the Cauchy-Schwartz inequality.

Considering one of the two layers is often more active relative to the other more passive layer at some control section, the control condition for that active layer i, based on its average velocity u_i would read as $F_i^2 = K_i$, in some analogy to Pawlak and Armi (1997), who used this form for single-layer control where shear effects account for the fact that $K_i < 1.0$.

In the two-layer stratified case with shear, we propose to correct the average velocity based Froude-number F_i^2 by dividing it with either the second order (M) or the third order (E) moments of the vertical velocity profile at the control sections where one layer is usually more active but with intense shear. Variation of F_1^2 through the contraction and F_2^2 over the sill for the three different layer approximations is shown together with the corrected estimates F_i^2/M and F_i^2/E for each layer i in the zoomed viewports of Fig. 4a. Two dimensional representation of the corrected F_1^2/M within the contraction region according to the streamline-based layer approximation is displayed in the colored viewport of the same figure.

With respect to the actively flowing layer, the peak values for G^2 are always located downstream (relative to the dominant layer velocity) of the topographic control points, as a result of frictional effects. Similar results were also shown by Pratt (1986) for frictional flows past a sill and for flows through a contracting channel by Winters and Seim (2000).

Estimates of the peak values of G^2 over the sill significantly differ for the three alternative layer approximations. It reaches and exceeds the critical value, $G^2 \geq 1$, for the streamline- and salinity-based layer approximations, while it remains below the critical value, $G^2 < 1$, for the velocity-based layer definition. M and E corrections lead

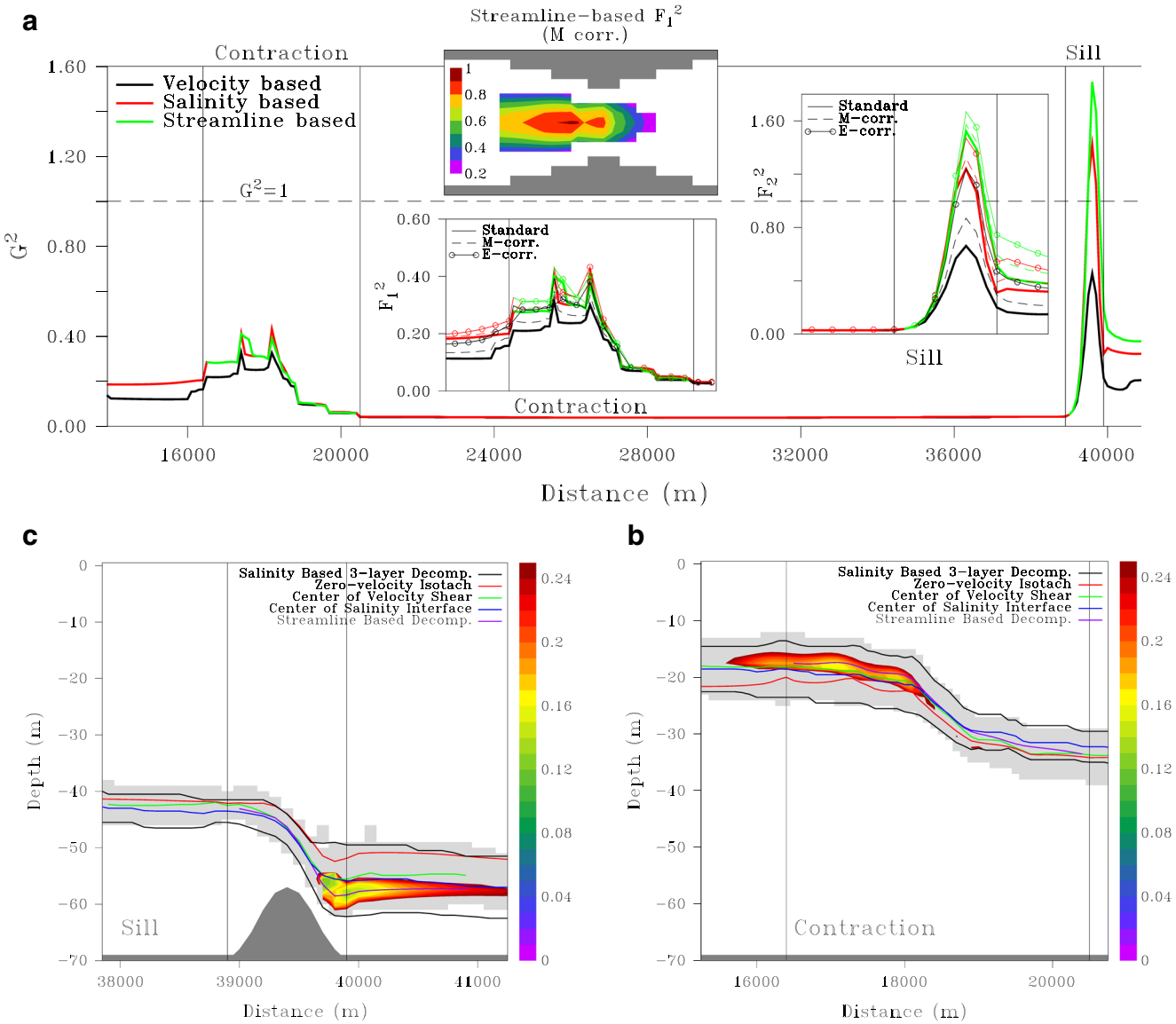

Fig. 4 (**a**) Along-channel variation of the two-layer composite Froude-number (G^2) calculated from velocity-, salinity-, and streamline-based layer approximations and standard, M- and E-corrected layer ($i = 1, 2$) Froude-number (F_i^2) estimates for the idealized model. Estimates based on three different layer approximations near the contraction and sill for respective active layers, as well as the horizontal variation of the M corrected F_1^2 based on the streamline method, are shown in the three viewports. Near the contraction (**b**) and the sill (**c**), laterally averaged variations of the salinity interface obtained with a three-layer decomposition are displayed. Velocity shear (*gray shade*) and its centerline, zero-velocity line and the streamlines used for the two-layer approximation, are shown, with the mid-section gradient Richardson number estimates (*color*) superposed within the salinity interface

to higher estimations when applied to the Froude-number F_2^2 and become more decisive as the defined lower-layer penetrates up further into the velocity shear region (Fig. 4a, c). For the sill region, even for the most unfavorable layer definition based on velocity, E-corrected estimation indicates a control condition immediately after the sill crest with $F_2^2 > 1$. Based on the two-layer Froude-number estimates, it can be confidently stated that hydraulic control exists at the sill.

Through the contraction, peak values of the composite Froude-number remain at subcritical level with $G^2 < 1$. Independent of the method used, the interface is found to be close to the center of the velocity shear. As a result, the M and E corrections do not lead to a significant increase in F_1^2, which appears to be the larger component (Fig. 4a, b). The horizontal distribution of M-corrected streamline-based F_1^2 computed at locations across the contraction region shows near-critical values within the central part of the

upper-layer flow, displayed in the color insert of Fig. 4a. Despite these complementing results on horizontal and layer averaged values of F_1^2, the existence of hydraulic control at the contraction can not be clearly established, perhaps because of the insufficiency of the two-layer approximation or the resolution of the model.

Checking the sensitivity of the estimates, we observe that the change from velocity- to streamline-based approximation results in a decrease of southward flux by less than 2.6 % and a decrease in the actively flowing upper-layer thickness by about 11.7 % leading to a small change at the peak G^2 value within the contraction region. Omitting completely this partially recirculated southward flux, an increase of 25.2 % is obtained in G^2. Finally, it can be said that despite the various corrections, the F_1^2 computed from cross-sectional average properties at the contraction remains as low as 0.45. We note however, by examining the horizontal distribution of Froude-number at every horizontal grid point (not shown), that the local value at a horizontal grid point downstream of the contraction approaches but still remains below the critical value of $F_1^2 = 1$. Using the streamline- versus velocity-based layer separation in the sill region results in a decrease of 33.2 % in the thickness of the actively flowing lower-layer and a boost of 125.6 % in the value of G^2, while excluding only 11.7 % of the lower-layer flux corresponding to the recirculated upper-layer flow. The streamline-based approximation in the sill region yields a rather uniform lower-layer, so that F_2^2 is relatively less affected by shear correction, setting an upper bound for the velocity- and salinity-based estimates with M and E corrections.

Based on many years of observations (Latif et al. 1991; Özsoy et al. 1998, 2001), it has been anticipated that a unique maximal-exchange regime could exist in the Bosphorus, and especially motivated by the analysis of Farmer and Armi (1986) for a two-layer strait flow between a contraction and sill, where the established hydraulic controls could uniquely determine the exchange between two reservoirs under certain conditions, which in fact are applicable to the Bosphorus.

The ability of the idealized model to represent some of the known features the Bosphorus Strait appear remarkably well, such as the sharp changes at the sill, contraction and south-exit, the interface thickness, and the sea-level difference between the two ends. However, not all expectations based on earlier observations can be confirmed by the results from a simplified model of the actual strait, and this is particularly true with respect to hydraulic controls. Two-layer composite densimetric Froude-number calculations based on the ideal model results support these expectations at the sill, as well as the Marmara Sea exit, where hydraulic controls with transition to a super-critical regime $G^2 > 1$ can be shown, but the same can not be demonstrated by the two-layer criteria at the contraction. Despite relatively rapid changes near the contraction of the depth and thickness of the interface and the free-surface elevation, akin to the observed properties reported for the Bosphorus, it is difficult to show Froude-number criteria satisfied. We also note that the two-layer Froude-number calculations based on two-layer model results of Oğuz et al. (1990) and observations by Gregg and Özsoy (2002) were also not able to show hydraulic transition at the contraction region. It is quite possible that, like most low-order formulations of complex physical processes, the two-layer composite densimetric Froude-number does not fully answer our inquiry to establish hydraulic controls at the contraction, but it does allow to establish hydraulic controls at the sill and the southern-exit to the Marmara Sea.

The maximal-exchange solution of Farmer and Armi (1986) for a two-layer flow between a contraction and sill ensures subcritical conditions supporting interfacial stability between the control sections. The theory implies supercritical, consequently unstable conditions in the region external to the controls. The streamline-based boundary of the active layers is located at the center of the unstable region with $R_i < 0.25$, past the contraction and the sill regions, as shown in Fig. 4b, c. In the potential area of shear instability south of the contraction in the Bosphorus, billows in the Bosphorus reminiscent of Kelvin-Helmholtz instability were observed (e.g., Gregg and Özsoy 2002). These results show low interfacial stability both at the contraction and the sill regions, supporting possible mechanisms of control, which unilaterally can be shown for the sill, but not for the contraction by two-layer criteria. The latter was proposed (Gregg and Özsoy 2002) to have frictional controls different from the sill case. We leave further discussion to the realistic case where we take up the question later.

3.2 Sensitivity to initialization

Radiation boundary conditions for salinity and $3d$-velocity components at the south and north open boundaries allow the model to settle to a steady-state after the LE initialization, while the barotropic south-north component $\bar{v}$ specified at the open boundary maintains the solution. The upstream specification of open boundary conditions ensures information travel outwards from the model domain except during inflows, when boundary values are implemented. Therefore, it is ensured that the steady-state solution only depends on the initialization.

The initial vertical front imposed at the strait mid section by the LE initial condition goes through stages of gravitational adjustment, first becoming slanted, then the two tails reaching the respective reservoirs, passing through hydraulic controls and dissipative regions of

Table 1 Summary of the experiments with different initializations indicating the respective reservoir depth of the salinity interface and whether the two-layer stratification extends to the open boundary (OB) or not

Experiment	South reservoir		North reservoir	
	Interface depth	*Extends to OB*	*Interface depth*	*Extends to OB*
LE	Lock-exchange initial condition			
FO	14 m	✗	56 m	✗
M-STEP-08m	8m	✓	56 m	✗
M-STEP-14m	14m	✓	56 m	✗
M-STEP-24m	24m	✓	56 m	✗
M-STEP-32m	32m	✓	56 m	✗
B-STEP-64m	14m	✗	64 m	✓
B-STEP-56m	14m	✗	56 m	✓
B-STEP-48m	14m	✗	48 m	✓

hydraulic jumps, emerging as subcritical flows at the open boundaries where they are maintained by the radiation boundary conditions with upstream specification of values. Such well-behaved model solutions approach a final state with hydraulic transitions at the sill, contraction, and the southern exit (maximal-exchange configuration) in most cases, and demonstrate the efficiency of the applied boundary conditions.

In this section, the existence of a steady-state response is investigated for selected cases of initial reservoir and strait density stratification provided in Table 1, with step-wise initial configurations of the interface, with indicated depth at the reservoir. In addition to the reference LE, simulations M-STEP and B-STEP represent runs in which respectively the south or north reservoir is completely stratified, while FO represents the test case initialized with fronts at both reservoirs, in accordance with examples shown in Fig. 5.

Differences from the reference LE initialization case are indicated in the top and bottom panels of Fig. 6, respectively showing the position of the $S = 28.5$ salinity contour (for practical reasons assumed to represent the interface) and the layer fluxes (Q_{upp}, Q_{low}) after steady-state has been reached. It is clear from the results that the solutions between the hydraulically controlled sections of the Marmara Sea exit and the northern sill remain almost identical for most of the cases as the depth of the interface either in the south or north reservoirs are varied. Significant differences in behavior are found, however, when the thickness

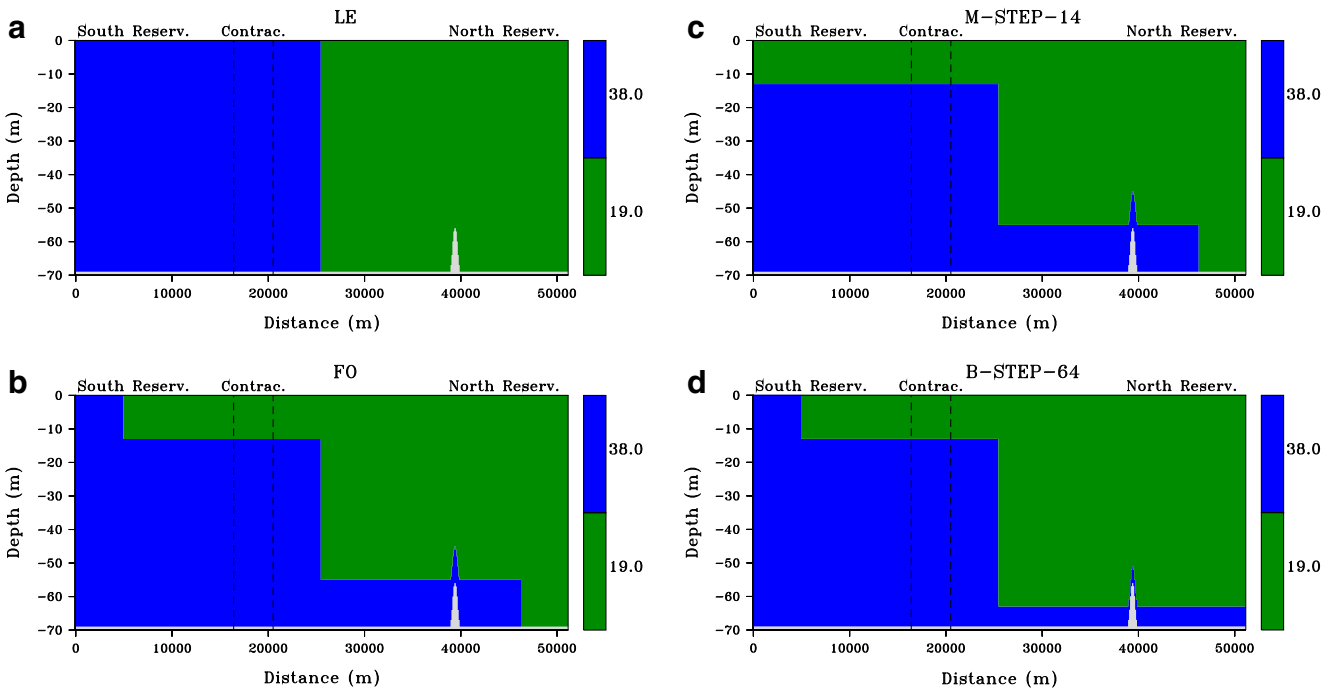

Fig. 5 Along channel salinity fields for the (**a**) lock-exchange (LE), (**b**) fronts-only (FO), (**c**) M-STEP-14 and (**d**) B-STEP-64 initialization schemes of the idealized model (M and B prefixes implying completely stratified conditions at either the south or north reservoirs)

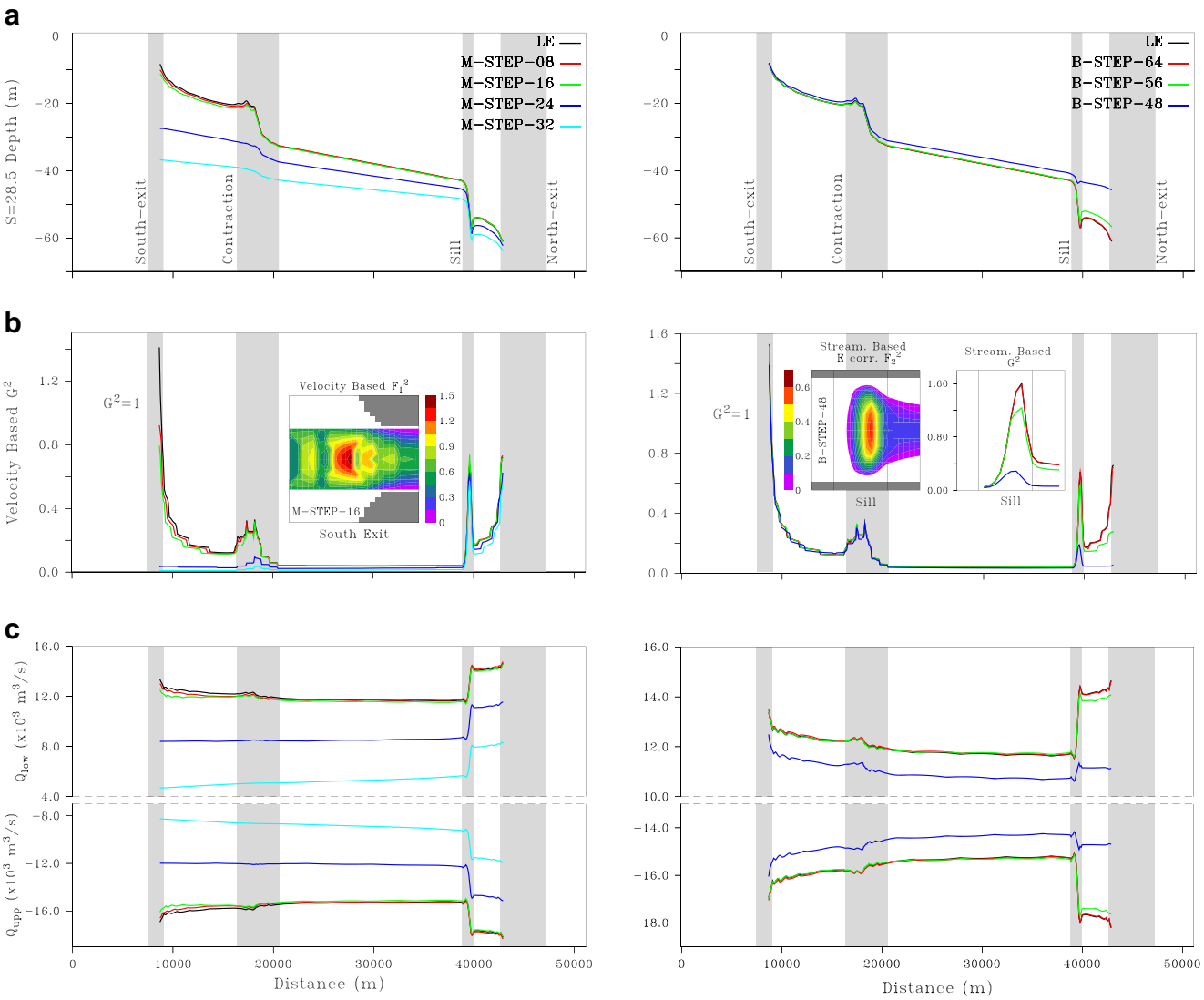

Fig. 6 Investigation of initialization sensitivity of the ideal model with completely stratified south and north reservoir, with layer properties obtained by the zero-velocity method of layer separation, described for the M-STEP (*left-hand-side panels*) and B-STEP (*right-hand-side panels*) cases compared with the LE solution: The panels (color codes given in (a)) show along-channel variations of (**a**) laterally averaged depth of the $S = 28.5$ iso-surface, (**b**) estimates of the two-layer G^2, with the insets showing two-dimensional distributions of the velocity based F_1^2 for the M-STEP-16 case at the south exit (lhs) and streamline-based G^2 for the three B-STEP cases, streamline-based horizontal variation of the E-corrected F_2^2 for the B-STEP-48 case over the sill (rhs), (**c**) upper (Q_{upp}), and lower layer (Q_{low}) fluxes for the above cases

of the upper layer at the Marmara Sea side (M-STEP cases, interface depths 24 and 32 m) or the thickness of the lower layer on the Black Sea side (B-STEP cases, interface depth 48 m) exceed certain limits, i.e., when the controls on either side are drowned by the reservoir conditions. It is significant that the layer volume fluxes are significantly altered in the drowned cases in which the former controlled solutions no longer exist. In the rest of the solutions excluding drowned cases, and disregarding small differences in the end regions external to the northern and southern controls, the steady state, maximal-exchange regime as proposed by Farmer and Armi (1986), appears to survive and produce almost identical results.

The loss of controls at either the south or north geometric transition regions is displayed by the two-layer estimates of G^2 given in Fig. 6b, in which the definition of the upper and lower layers is based on the flow direction, and the flow outside of the inner-channel width is excluded from the computation. With Froude-number estimations exceeding the critical value $G^2 = 1.0$, two-layer hydraulic controls are apparent at the south-exit for the reference case LE and for interface levels below 16 m at

the south reservoir. For the solution with Marmara interface depth of 16 m, the two-dimensional distribution of F_1^2 displayed in the color insert indicates values reaching 1.5 near the Marmara exit. For the drowned cases with Marmara interface depths 24 and 32 m, Froude-numbers at the exit remain far below critical values, showing that the exit hydraulic control is completely lost. A local peak of G^2 is always observed at the contraction, and as noted earlier (Fig. 4a), it remains subcritical in terms of average properties and barely reaches a critical value at some local grid point for the non-drowned solutions. For the drowned cases when control is lost at the exit, even when a E correction is applied to the dominant term F_1^2 and with the most favorable layer definition, local estimates of G^2 remain below a value of 0.2, suggesting that the contraction does not take over the control role lost by the south exit.

When the Black Sea side is stratified, G^2 computed according to flow direction does not reach critical value of 1.0 at the sill, as shown in Fig. 6b. However, criticality is reached within the lower layer such that $F_2^2 > 1$ in the reference case LE and for the cases with interface depth at 56 or 64 m when layer definition is either salinity- or streamline-based. In the drowned case with Black Sea interface depth at 48 m, streamline-based peak G^2 value at the sill is still quite small, and even with the E correction accounting for vertical shear, the maximum value of the Froude-number at any local grid point is not greater than 0.7, suggesting the loss of hydraulic control at the sill.

4 Realistic model

As described in Section 2, basic runs of the model with realistic model geometry were made in accordance with selected basin water properties listed in Table 2. Runs 1-4 correspond to LE initial conditions with typical uniform salinity and temperature values of $S = 38.0$, $T = 13.0$ °C in the south and the cases of $S = 17.6$, $T = 4.0/14.0/24.1$ °C in the north, amounting to density differences of 14.74–18.22 kg/m^3. The variation in north side temperatures in runs 1–3 attempts to represent seasonality in the Black Sea. The net barotropic flux in runs 1–3 is set to $Q_{\text{net}} = -9.5 \times 10^3$ m^3/s (negative towards Marmara), corresponding to the mean annual volume flux of about -300 km^3/year quoted by Ünlüata et al. (1990), and changed to $Q_{\text{net}} = -5.6 \times 10^3$ m^3/s in run 4 to represent conditions similar to September 1994 measurements of Gregg and Özsoy (2002).

To avoid instabilities during start-up, LE simulations are started with a very small baroclinic time-step of $\Delta t = 1.75$ s with enhanced vertical mixing, adjusted later to 4.0 s after the first day of the run, continued for a total duration of 5.55 days with an external time-step that is 20 times smaller throughout the whole simulation. This two-step approach is useful in decreasing the long computational time due to the initial sharp contrasts in water properties and the narrow, complex strait geometry.

The second group, runs 5 and 6, simulates stratified reservoir conditions specified with depth profiles of temperature and salinity at the two sides of the initial front, based on the September 1994 observations of Gregg and Özsoy (2002). Accordingly, stepwise profiles with constant values of $T = 22.5$ °C, $S = 23$ above 11 m and $T = 13$ °C, $S = 38$ below 25-m depth, with linear change in between, were specified on the Marmara side, while constant salinity of $S = 17.6$, and $T = 24.1$ °C in the first 20 m followed by a linear decrease to $T = 7.0\,°C$ at 45 m, remaining the same below, was assumed to represent the cold intermediate water (CIL) in the Black Sea. A mixed radiation and nudging open boundary condition was applied with a nudging coefficient of 0.1 day for the outflow and 0.01 day for the inflow while forcing the laterally uniform salinity and temperature fields detailed above.

The stratified solution, run 5, is restarted from the steady-state of run 4 and lasted for a total duration of 23.15 days with the same configuration except for the

Table 2 Temperature, salinity initial values, density differences, and net volume fluxes for the Bosphorus realistic model runs 1–4 (LE initialization); run 5 and run 6 (stratified boundary conditions)

Run	Salinity, S		Temperature, T (°C)		Density difference, $\Delta\rho$(kg/m^3)		Net flux, Q_{net}(10^3 m^3/s)
	Marmara	Black Sea	Marmara	Black Sea	Initial	Steady-state	
run1	38.0	17.6	13.0	24.1	18.22	15.70	−9.5
run2	38.0	17.6	13.0	14.0	15.93	13.73	−9.5
run3	38.0	17.6	13.0	4.0	14.74	12.72	−9.5
run4	38.0	17.6	13.0	24.1	18.22	15.78	−5.6
run5	stratified (RUN4 Steady State)				15.78	9.32	−5.6
run6	stratified (RUN1 Steady State)				15.70	9.34	−9.5

modified tracer forcing. Similarly, run 6 is restarted from run 1 for $Q_{\text{net}} = -9.5 \times 10^3 \text{m}^3/\text{s}$.

Temporal evolution of the mean kinetic energy per volume for run 5 is given in Fig. 7a together with the evolution of volume flux at the boundaries and through a mid-strait section in Fig. 7b. The final steady-state is achieved by successive restarts. The first stage, SPIN, starts from the LE initial condition with enhanced mixing and appropriate small time-step, followed by the STEADY stage corresponding to run 4 with GLS mixing, and is continued with the NUDG stage corresponding to run 5 with the stratified reservoir conditions.

The adjustment of the model from the LE release is quite fast and is followed in the second stage by adjustment to a more energetic state through turbulent mixing, despite the lowered net volume flux. In the last stage, starting from day 5.55, large amplitude oscillations occur due to adjustment to the stratified basin conditions, eventually settled to a less energetic state (due to the decrease in $\Delta\rho$) in a matter of 10 days. Oscillations are also observed in the mid-strait volume flux, but in a weaker manner, with residual oscillations of less than 0.75 % of the final net volume flux.

Two-layer volume fluxes of the upper and lower layers, Q_{upp} and Q_{low}, respectively, are calculated according to the flow direction considering the along-channel velocity on the model grid (see Fig. 2). Three-layer decomposition into top, bottom, and interface volume fluxes, Q_{top}, Q_{bot}, and Q_{int}, respectively, is based on delineating layer limits with salinity difference within 10 % from the reference top and bottom values and assigning the remaining region to the interfacial layer.

4.1 Uniform reservoir conditions

In runs 1–3, the net volume flux is kept the same, while changing the Black Sea water temperature, influencing only the density difference (Table 2). The steady-state characteristics are almost identical for these cases, apart from small differences in layer fluxes and free-surface variation along the strait. These results indicate minimal influence of the seasonal changes in temperature.

We note that stratification effects in both reservoirs are missing from the above runs, since uniform properties are imposed in the Marmara and Black Sea basins. Yet, the successful predictions exemplified by run 1 in Fig. 8 recall some observations in the strait (Gregg et al. 1999; Gregg and Özsoy 2002; Özsoy et al. 2001) indicative of similar features, such as the thickness of the interface, the response to topographic variations, the gradual changes of properties in layers by turbulent mixing and entrainment mechanisms, the rapid changes at the south-exit and the contraction region, the overflow of the lower-layer flow over the north sill

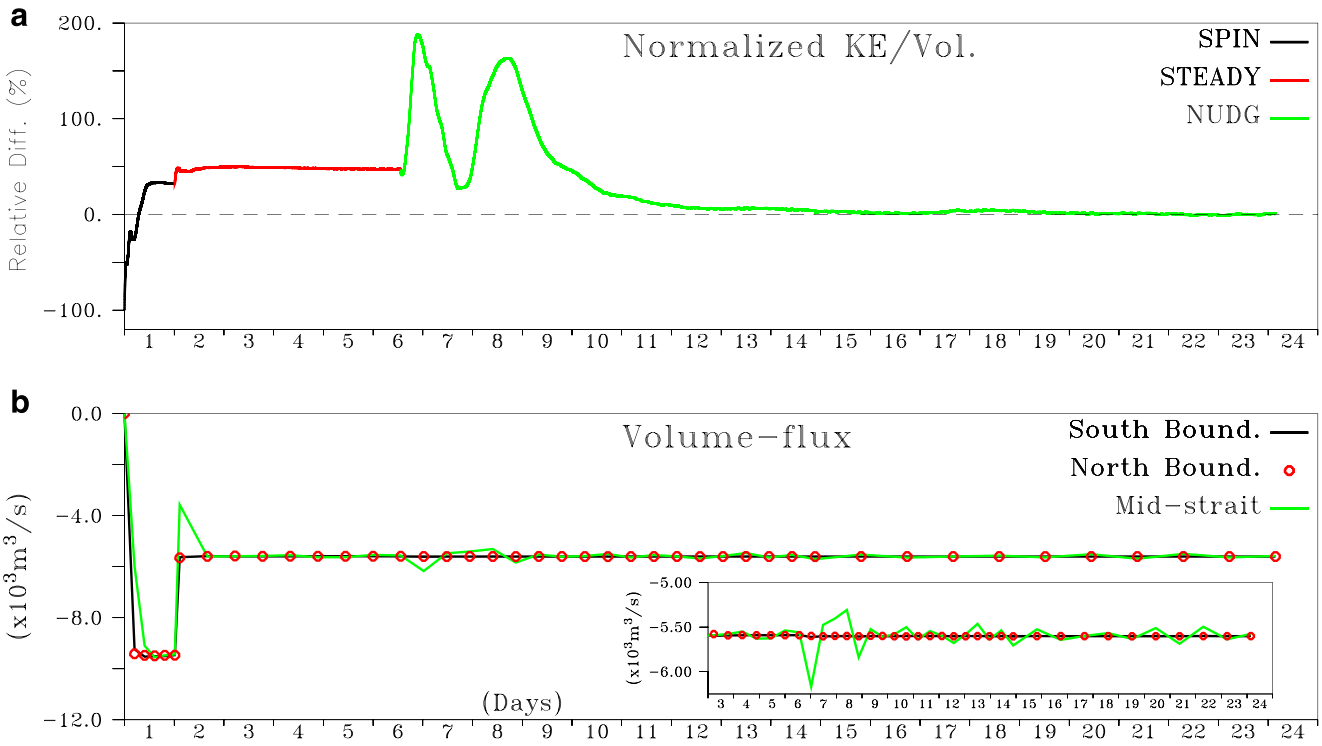

Fig. 7 Temporal evolution of (**a**) mean kinetic energy per volume, computed relative to the final state, (**b**) volume flux at the open boundaries and at a mid-strait section for run 4, comprising SPIN and STEADY stages, and run 5 (NUDG stage) with nudged open boundaries which is a stratified solution started from the steady-state result of run 4. The inset shows a zoomed view of the oscillations after day 3

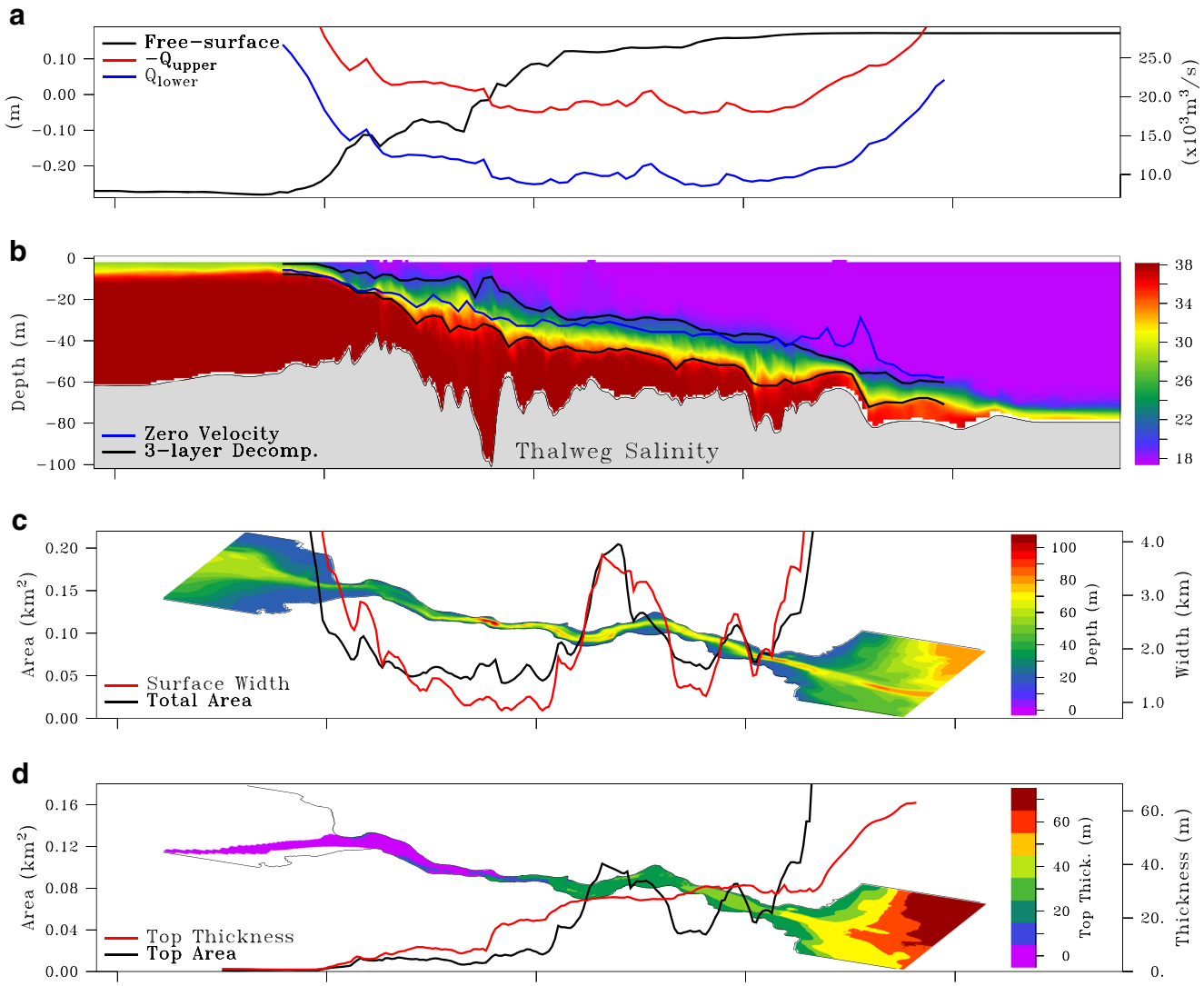

Fig. 8 (**a**) Along-channel variation of the free-surface elevation, upper and lower layer fluxes. (**b**) Salinity section showing the three-layer decomposition based on salinity and the zero-velocity isotach along thalweg. (**c**) Variation of the cross-channel area and surface width; layer area and thickness for the (**d**) top, (**f**) bottom layers and south-north layer velocity and salinity for the (**e**) top, (**g**) bottom layers (run 1)

followed by a hydraulic jump, and its final spreading on the Black Sea continental shelf as a thin layer. The zero-velocity contour in Fig. 8b is bounded by the interface layer in the southern part of the strait and gradually rises above the interface before reaching the northern sill, as suggested by Tolmazin (1967, 1985) and also indicated by observations of Gregg and Özsoy (2002). Sea surface height in Fig. 8a varies smoothly in the northern part of the strait, until reaching the area of the contraction, where it undergoes a significant drop, finally reaching the south end of the strait with a sea level drop of $\Delta\eta = 44$ cm between the Black Sea and the Sea of Marmara, in agreement with observations.

Significant variations occur in the magnitude of the layer volume fluxes along the strait excluding the exit regions, respectively amounting to $Q_{\text{upp}} : 18,650-22,700$ m^3/s and $Q_{\text{low}} : 9200-13,300$ m^3/s as shown in Fig. 8a. Within the strait the ratio $Q_r = |Q_{\text{upp}}|/|Q_{\text{low}}|$ varies between 1.7 and 2.1. We also note that the average volume fluxes presented in Table 3 are computed as the average of a 2-km section at the middle of the strait, where they are relatively constant.

The along-strait variations of geometric and layer properties for run 1 are illustrated in Fig. 8c–g. The strait cross-sectional area and the width at the surface given in Fig. 8c illustrate the various undulations and bends in channel geometry. The narrowest part of the strait occurs in the southern part, including the main contraction, where the depth also reaches its maximum. Halfway north of the strait, there is a widening region followed again by alterations of narrow and wide parts further north.

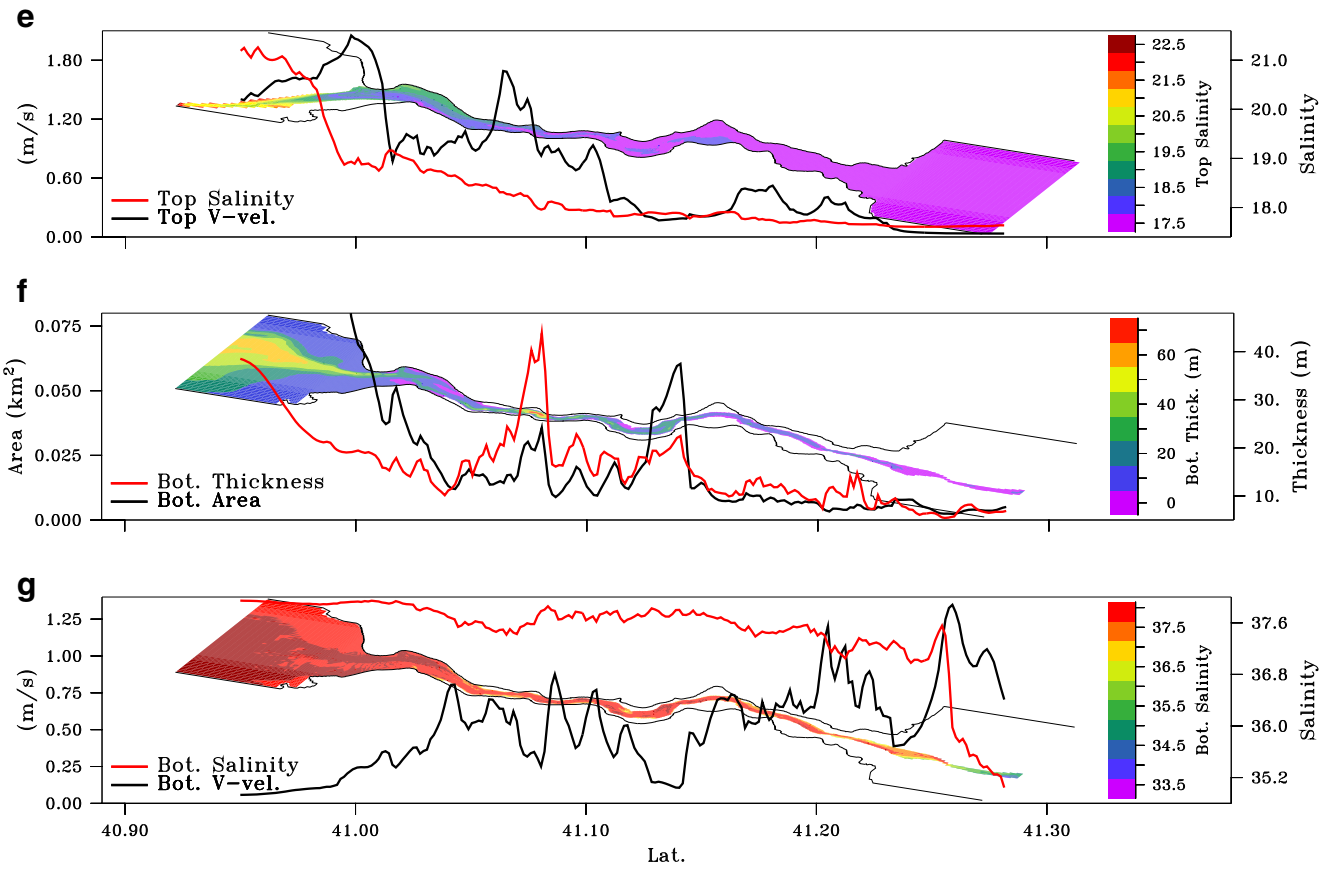

Fig. 8 (continued)

The top and the bottom layers exhibit important changes in response to geometric controls. Figure 8d indicates that the top layer thickness varies in rapid adjustment to changes in width, upon entering the strait from the Black Sea, as well as upon entering the narrow section about halfway along the strait, with the largest decrease occurring at the contraction. From this point towards the south-exit region. The thickness of the top layer remains almost constant.

In Fig. 8e, it is shown that the top layer reaches the contraction region without significant change in salinity, but speeds up and becomes strongly modified by entrainment processes within the southern part of the strait and upon entering the Marmara Sea. The cross-sectional average of the top-layer velocity is less than 0.5 m/s in the north part of the strait, but is rapidly accelerated to ∼1.0 m/s upon entering the contraction region, reaching a peak value of ∼1.6 m/s (velocity magnitude) further south of the contraction, followed by a return to the value of ∼1.0 m/s in the widening section approaching the exit. The top layer penetrates into the Marmara Sea as a jet with surface flow speeds as high as ∼2.5 m/s (not shown).

Table 3 Net flux, layer fluxes (10^3 m^3/s), and sea-level differences (m) for the Bosphorus realistic model runs

Run	Q_{net}	2-layer		3-layer		Q_{exc}	$\Delta\eta$
		Q_{upp}	Q_{low}	Q_{top}	Q_{bot}		
run1	−9.5	−19.2	9.7	−16.1	6.8	28.9	0.44
run2	−9.5	−18.3	8.8	−15.3	6.2	27.2	0.40
run3	−9.5	−17.9	8.4	−15.0	5.8	26.2	0.37
run4	−5.6	−17.1	11.5	−14.2	8.4	28.6	0.41
run5	−5.6	−15.3	9.7	−12.8	4.4	25.0	0.22
run6	−9.5	−17.8	8.3	−14.6	4.0	26.1	0.26

The bottom layer, Fig. 8f, fills the whole width and depth of the cross-section at the southern part of the strait, but becomes completely confined inside the deep inner-channel at the northern part of the strait. Contrary to the top layer which exhibits a distinctive difference between the north and south parts of the strait, the bottom layer is directly affected by the depth variations. The average velocity is strongly influenced by the bottom geometry but salinity remains only slightly modified until reaching and overtopping the sill, as shown in Fig. 8g. The greatest change in bottom layer salinity occurs by entrainment in the hydraulic jump region past the sill. At the exit region, the deep

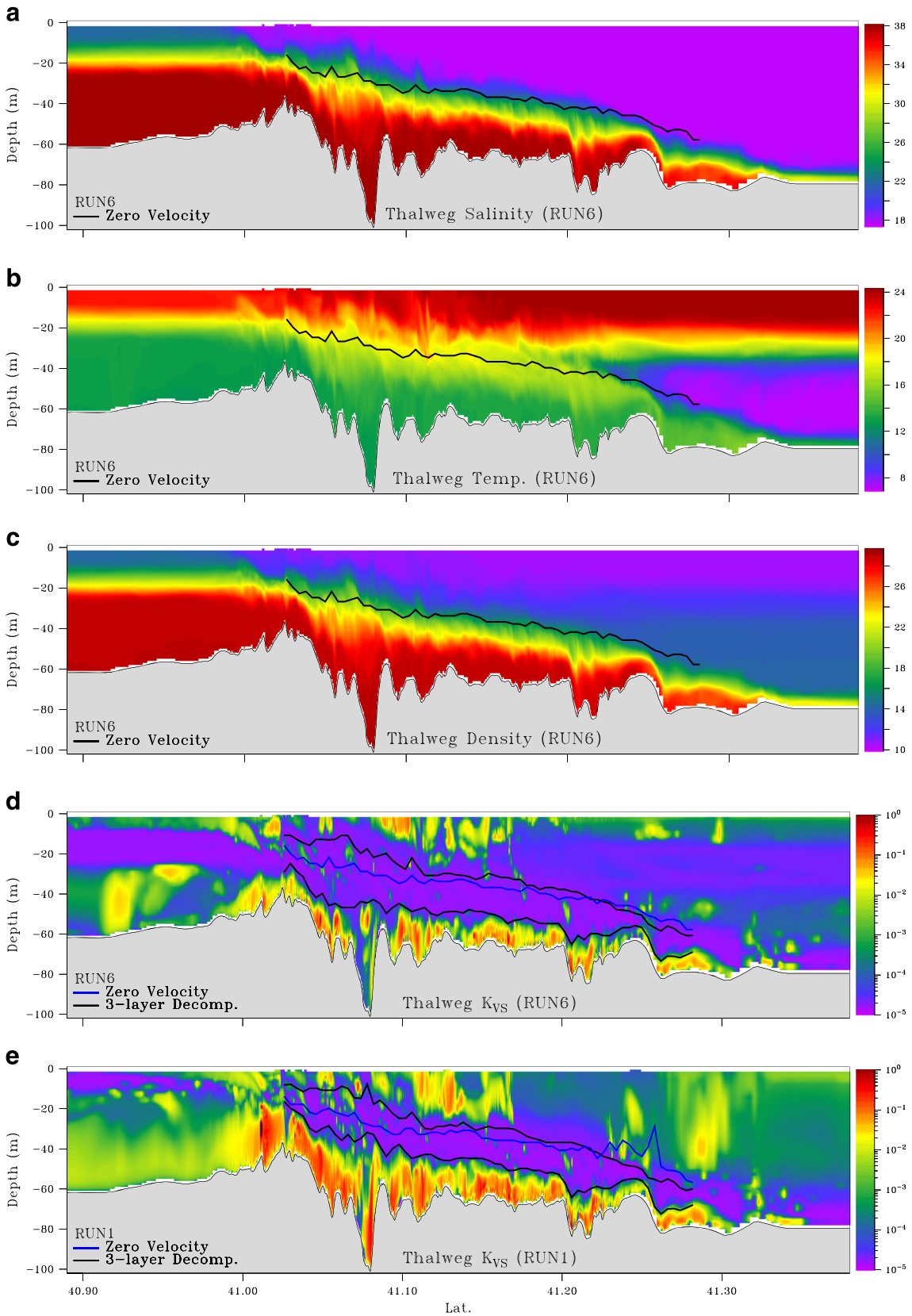

Fig. 9 Along-channel salinity (**a**), temperature (**b**), and density (**c**) with the zero-velocity isotach for run 6 and the vertical turbulent diffusivity of temperature and salinity, together with the salinity-based three-layer decomposition and the zero-velocity isotach for (**d**) run 6 and (**e**) run 1

inner-channel expands, and the bottom-layer decelerates while climbing over the north sill, still confined within canyon, and reaches a peak layer averaged flow speed of ∼1.4 m/s. The ensuing local features of the flow along the canyon joining the Black Sea shelf, captured by Özsoy et al. (2001) and Dorrell et al. (2016), are outside the maximum extent of the model domain.

4.2 Stratified reservoir conditions

In this section, we initialize the model with stratified basin properties, based on observed profiles of temperature and salinity in the Marmara and Black Seas. As in the case of uniform reservoir conditions, the model solutions under the stratified boundary conditions qualitatively reproduce many features reported in the earlier observations (e.g., Özsoy et al. 2001; Gregg and Özsoy 2002) such as the adjustment of the flow according to the stratification of the neighboring seas, the wedge-shaped upper and lower layers with distinctly different properties, the apparent hydraulic transitions at the contraction and sill, the thin surface layer outflow into the Marmara Sea, the sill overflow, and subsequent adjustment on the Black Sea shelf, for instance in run 6 (Fig. 9a, b).

Yet, the introduction of stratified reservoir conditions in both Marmara and Black Seas had the greatest impact on Bosphorus model results obtained so far. In particular, one of the greatest changes in behavior appeared to be a consequence of the cold intermediate layer (CIL) entering the strait from the Black Sea and coming into direct contact with the interfacial layer separating it from the warmer waters of the undercurrent, impacting the stratified turbulence and therefore mixing characteristics of the interfacial layer, as shown in Fig. 9b, c, d. The major difference in terms of salinity has been observed in the Marmara side where the increased interface depth results in a significantly smaller average density difference between the two reservoirs complementing the effect of the CIL.

When one considers the density (Fig. 9c), it is observed that the strong density stratification on the Black Sea side has a suppressing effect on interfacial turbulence. This is clearly seen from the comparison of Fig. 9d, e displaying vertical turbulent diffusivity for runs 1 and 6, with reduced magnitude of the diffusion coefficient at around mid-depths where the CIL penetrates into the Bosphorus below the warm surface water and increases static stability of the water column. The suppressed mixing is evident in the stratified case of Fig. 9d, especially at mid-depth. Similarly, within

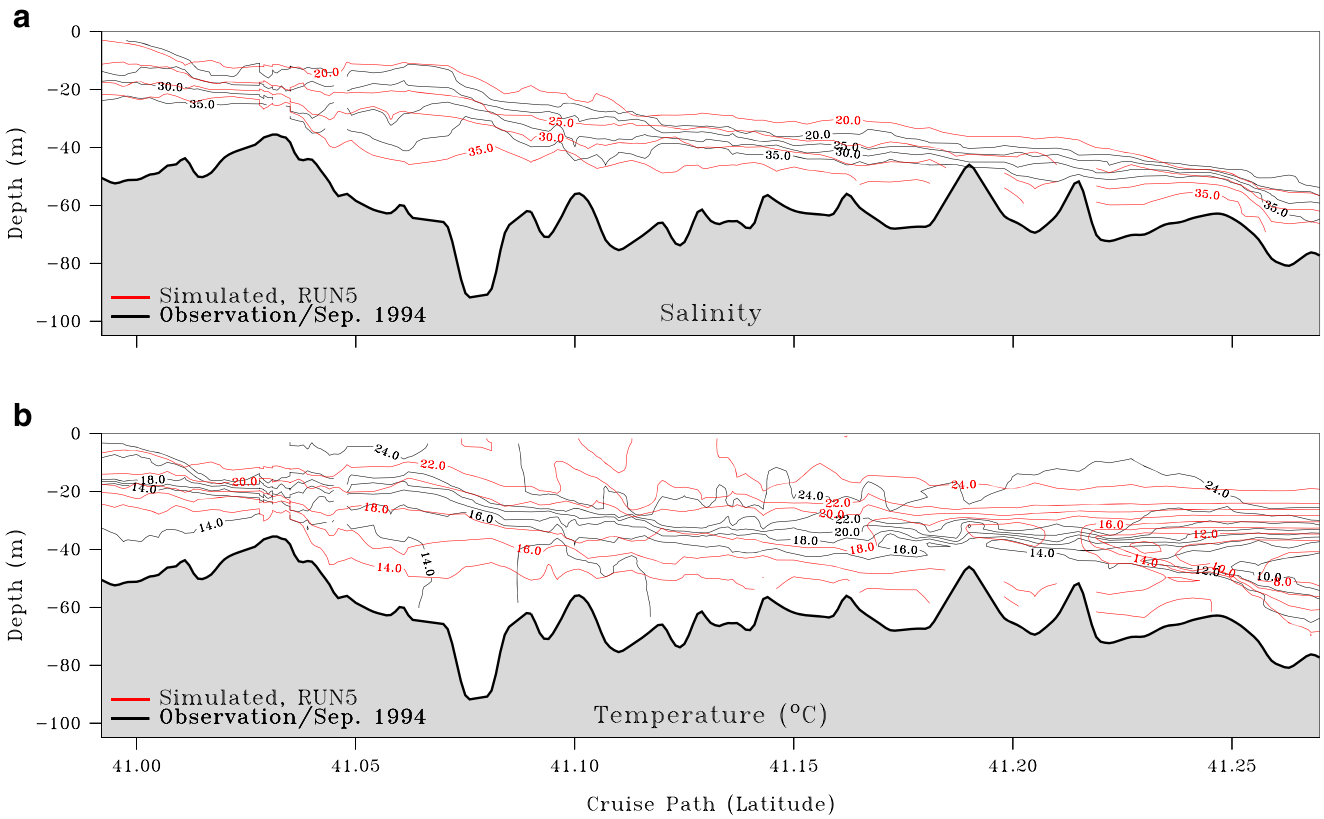

Fig. 10 Comparison of the simulated (run 5) salinity (**a**) and temperature (**b**) fields with the observations through the strait; field data consists of 113 ctd stations obtained between 7 and 9 September 1994 by Gregg and Özsoy (2002)

the stratified upper-layer of the Marmara Sea, increased static stability is also evident resulting in suppressed mixing in the sub-surface waters.

Overall, we see that one of the two resultant effects of stratification in the adjacent reservoirs is the significant decrease of $\Delta\eta$ between the two basins compared to the uniform reservoir solution (run 1), in consequence to the reduced density difference between reservoirs in the stratified solution (run 6). The second significant effect observed in the stratified solution (run 6) is the thicker interface formed within the strait compared to the unstratified case (run 1).

We test the realism and verify the predictive capacity of the model by comparing results with selected observations obtained during measurement campaigns. Parameters of run 5 have some correspondence to the moderate barotropic flow conditions during the extensive measurements obtained by Gregg and Özsoy (2002) in September 1994. Comparisons of the model produced salinity and temperature fields with measurements of September 1994 (Fig. 10) indicates successful simulation of the basic characteristics of the exchange flow in the Bosphorus Strait. Briefly, the model is able to establish and preserve stratified water characteristics in the neighboring seas and correctly estimates the intrusion of the CIL into the Bosphorus Strait. The slope of the interface from contraction to the north sill is in good agreement with the data and the abrupt change in the depth of the interface while passing through the contraction is very well represented. The overflow over the north sill and the following internal hydraulic jump is successfully demonstrated. The most prominent difference between the modeled solution and the observation is in the estimated thickness of the interfacial-layer between these two control sections, i.e., in the northern sector of the strait, where the observations suggest relatively sharper gradients at the interface. The larger interface thickness in the model appears to be related to the contribution of horizontal diffusivity to vertical mixing, a byproduct of the *s*-coordinates used by ROMS, which becomes more pronounced when stratified boundary conditions are taken into account.

A non-linear variation of sea level occurs along the strait, with successive rapid changes at the Marmara exit and the contraction region where the flow is anticipated to go through hydraulic transitions. An interesting result of including realistic vertical stratification in the adjacent seas is observed in terms of the free-surface response through the Bosphorus. In comparison to the unstratified case, the intruding CIL in the stratified case decreases the average density difference between the south and north reservoirs, as well as between the upper and lower layers, as indicated in Table 2, resulting in an overall decrease in the sea level difference between the two basins (Table 3). Comparing runs 4 and 5 with the same net volume flux, it can be observed that the sea-level difference across the Bosphorus is reduced by almost a ratio of one half, from 41 cm in the non-stratified case to 22 cm in the stratified case, consistent with the sea-surface height differences estimated by Gregg and Özsoy (2002) under similar conditions.

Runs 1–3 of Table 3 having the same net volume flux of $Q_{\text{net}} = -9.5 \times 10^3 \text{m}^3/\text{s}$ but different initial values gives a linear relation with correlation coefficient $R^2 = 0.999$ between steady-state $\Delta\eta$ and $\Delta\rho$, which would yield an empirical estimate of $\Delta\eta = 24.8$ cm for run 5 based on run 4, considering the density difference of of $\Delta\rho = 9.32\ \text{kg/m}^3$. A similar calculation can be made for run 6 using run 1. For these two cases of different net fluxes, the modeled sea-level differences are 2.7 cm (run 5) and 2.6 cm (run 6) less than the linear estimates. There appears an additional decrease in sea-level difference as the intrusion of stratified waters from the Black Sea and the Marmara Sea evidently increase interfacial stability, and the frictional losses are decreased by suppressed vertical mixing, inducing smaller $\Delta\eta$ needed to overcome the density difference for a specified net volume flux.

4.3 Hydraulic control

It is not clear based on measurements if and where hydraulic controls exist in the Bosphorus. The hydraulic controls often were anticipated at locations where fast changes occur in channel geometry, but except for the northern sill, could not be positively demonstrated by the classical, simplified two-layer Froude-number calculations with layer-averaged properties, using the uniform flow and homogeneous layer assumptions Gregg and Özsoy (2002). In addition to the discrepancy with the classical theory, the Froude-number is often calculated from incomplete density and current data respectively obtained from the CTD and ADCP measurements, which often are not simultaneously recorded, or miss some velocity data near the surface and the bottom.

4.3.1 Two-layer approximation

The classical arguments for establishing the existence of hydraulic controls often have been based on estimates simply adding up the single-layer Froude-numbers squared $F_i^2 = u_i^2/g'h_i$ based on the average velocity and depth of each layer as if they were from a rectangular section, or alternatively, assigning a nominal thickness approximated by the layer area divided by the width for a variable depth section. For flows through variable cross-sections with transverse velocity variations, an improved approximation for the two-layer Froude-number computation is given by Pratt (2008):

$$G_w^2 = F_{1w}^2 + F_{2w}^2, \tag{3}$$

Table 4 Local Froude-number maxima at topographic barriers; two-layer composite Froude-number estimate by Pratt (2008)'s method (Std.-G^2), energy corrected estimate for the active layer (E-F_i^2), energy-corrected estimation for the actively flowing layer excluding sluggish currents (Active-F_i^2) and percentage of the actively flowing layer flux excluding the sluggish currents to the total layer flux (run 5)

Region	Max. Froude-number			Active layer	Act./Tot. layer flux
	Std. G^2	*E.-* F_i^2	*Act.* F_i^2		
South-exit	0.42	0.63	1.20	Upper	82.33 %
Üsküdar	0.35	0.60	1.18	Upper	82.46 %
Contraction	0.40	0.73	0.98	Upper	77.77 %
North sill	0.61	0.73	0.97	Lower	76.99 %

where $F_{iw}^2 = [w_l^{-1} \int (g' h_i / u_i^2) dx]^{-1}$ are the squares of the densimetric Froude-numbers for the upper and lower layers $i = 1,2$ respectively, expressed as the inverse of an integral across the entire flow area averaged over the width spanned by the interface w_l, such that u_i is the mean current speed and h_i the depth at position x across the section in each layer of the variable depth channel and $g' = g\Delta\rho/\rho$ is the reduced gravity.

Based on the experience with experimental data and model results, we employed two methods that ultimately could result in more realistic composite Froude-numbers providing a better assessment of the existence and localization of hydraulic controls in the Bosphorus Strait. The first one is the extension of Garrett and Gerdes (2003) formulation (as in Section 3.1) to apply an energy flux correction before carrying out Pratt's integration across the width, yielding two-layer Froude-number estimation of

$$F_{iw}^2 = [w_l^{-1} \int (E_i g' h_i / u_i^2) dx]^{-1}; \quad i = 1, 2. \tag{4}$$

A difficulty in substituting a numerical estimate in place of an analytical layer definition is the lack of a clear surface separating the layers, which complicates the use of w_l in the calculation of G^2. Therefore, a slightly modified calculation has been made for the upper-layer Froude-number F_{1w}^2 in which the upper-layer width w_1 is used instead of w_l (interface width).

A further significant improvement of the Froude-number computation was made by carrying out the numerical integration through the active zones of the individual layers across the section by excluding the sluggish parts of the layer flows. In the calculation of what we termed as the "active Froude-number," not only the zones of the layers with depth-averaged velocity vectors that were lower in magnitude compared to the cross-sectional average but also the zones with relatively insignificant volume fluxes were excluded from the computation.

The calculated composite Froude-number and ratio of active fluxes to the total fluxes (for run 5) are given in Table 4 for the regions where hydraulic control is inferred. The standard method for two-layer hydraulics approximation using the variable sections approach of Pratt (2008) fails to show criticality at the inferred locations. Applying energy flux corrections in account of vertical shear also is not sufficient to raise the Froude-numbers above the critical levels. The ratio of the active flux to the total flux is almost always above 75 % for these sections, such that the effect on the calculation of active F^2 is significant. Only by applying the method that selects the active areas as described above, we are able to observe that the northern sill, the main contraction, the headland at Üsküdar (historical Scutari), and the southern exit either pass or come very close to criticality conditions.

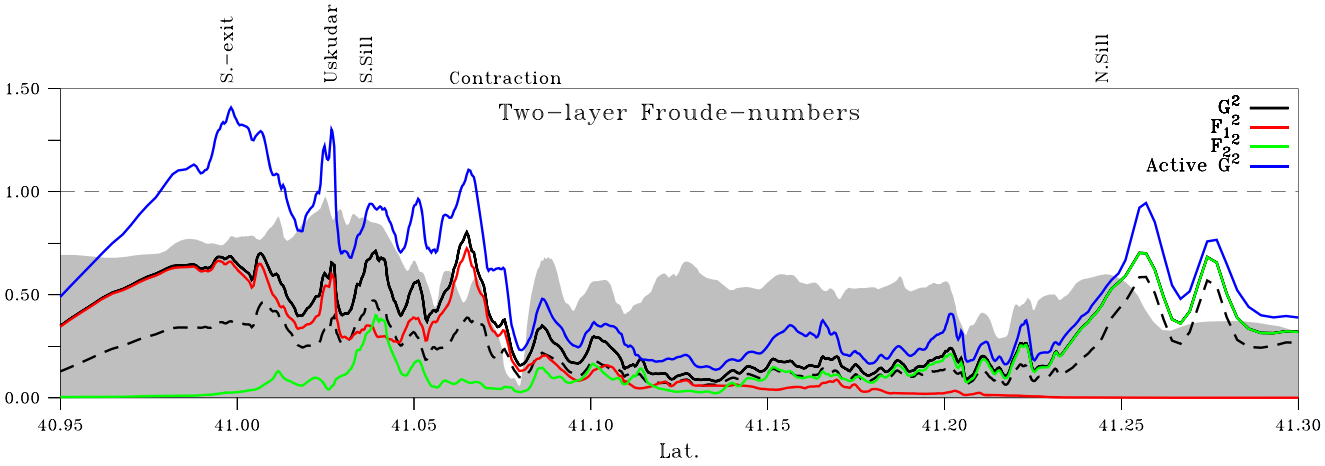

Fig. 11 Estimates of composite Froude-number, G^2, utilizing plain Pratt (2008) formulation (*dashed line*), energy-corrected cross-channel integrated Froude-numbers; F_1^2 for upper, (*red*) F_2^2 for lower (*green*), and total G^2 (*black*) based on Pratt (2008) and Garrett and Gerdes (2003) formulations; and "active" composite Froude-number, G^2, estimated by excluding the sluggish parts of the flow (*blue*) with the same method (run 5). The bottom topography is shown by the gray background

For the computations, the model output in the regular grid was transferred to two non-orthogonal curvilinear grids following the upper- and lower-layer flow paths determined by maximizing the average along-channel volume fluxes of the layers. The variation of the energy-corrected and "active" composite Froude-number G^2 estimates are displayed in Fig. 11 together with the "plain" estimates (dashed line) without the energy correction and the active flow approximation.

The along-channel variation of the "plain G^2" estimate plotted in Fig. 11 fails to confirm the existence of hydraulic controls anywhere, although local increases are observed at the Marmara exit, Üsküdar, the southern sill, south of the contraction, and following the northern sill. Between the contraction and the northern sill, the Froude-number has the smallest values, suggesting that the controlled sections are external to this domain. With the energy corrections, the composite Froude-number increases significantly, approaching the critical value, but not really reaching it at any location. Yet, when the "active" composite Froude-number for the actively flowing cores of the layers is computed, we start to see G^2 approaching unity in few locations; the south-exit, the headland at Üsküdar, the main contraction, and the north sill with peak values and henceforth hydraulic controls not exactly at the minimum depth or width locations but slightly past these constrictions as implied by Pratt (1986) for frictional controls (Figs. 11 and 12a–c). The existence of subcritical flow conditions between the contraction and the northern sill hydraulic controls confirms the establishment of the two-layer maximal-exchange regime through the strait.

The lee-side of the northern sill is the only place in the northern sector where the active composite Froude-number, G^2, rises towards a critical value, almost totally contributed by the hydraulically controlled lower-layer flowing inside a canyon. The controlled flow at the sill is immediately followed by a hydraulic jump, followed by a reformed flow, and later again a second sharp G^2 increase is observed. A similar, secondary peak of increased Froude number due to reformation of the flow past the primary hydraulic control and the subsequent hydraulic jump has also been noted by Dorrell et al. (2016) in the canyon flow north of the northern sill. The oscillatory trend in G^2 past the sill is sensitively connected to the fine-scale changes of the flow area of the canyon sloping down to join the Black Sea shelf, noted also by (Özsoy et al. 2001) in their Fig. 9 which is successfully preserved in our high-resolution model grid.

Horizontal variation of the volume flux vectors and F^2 is given in Fig. 12a–c for the actively flowing layers at the north-exit, contraction region, and the Marmara exit together with the active zone widths of the flow through which the integration of the Froude-number is carried out. Both fields are plotted on the non-orthogonal curvilinear grid, and the local maxima for the energy-corrected F^2 are marked with lines parallel to the cross-section of this curvilinear grid for the displayed layer.

Cycles of reformation and dissipation similar to those observed past the north sill are also seen south of the main contraction where the active G^2 approaches unity. Slightly past the contraction (Figs. 11 and 12b), there are oscillations where G^2 falls by dissipative mechanisms and again rises by the flow reforming, occasionally coming close but

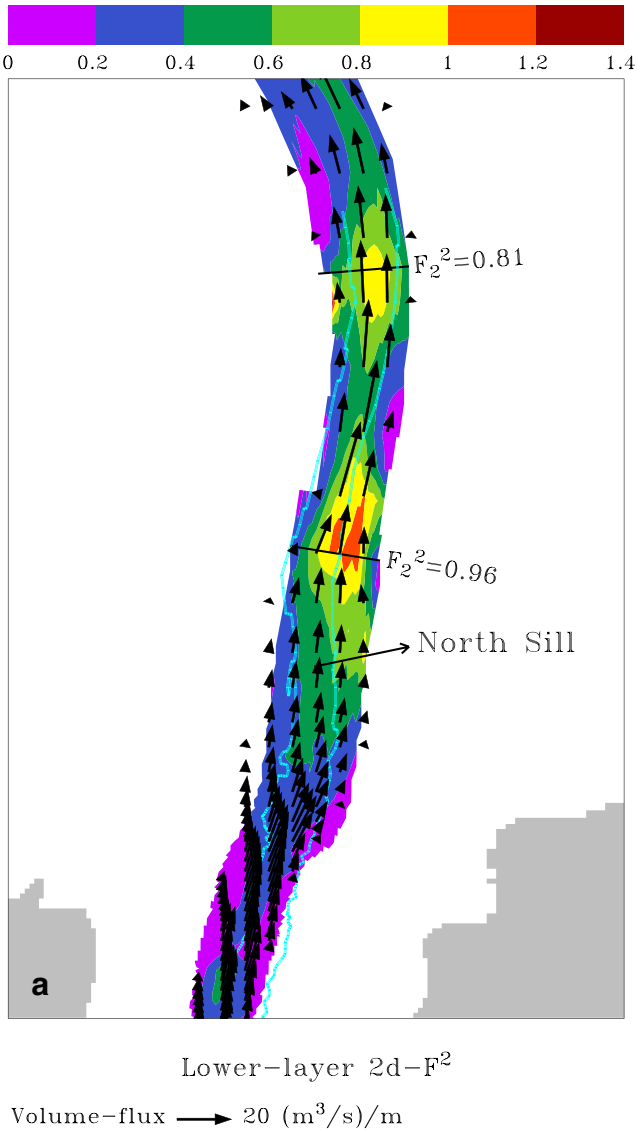

Fig. 12 Two-dimensional variation of the Froude-number for the active layers within the (**a**) Black Sea exit (*lower layer*), (**b**) contraction (*upper layer*), and (**c**) Marmara exit (*upper layer*) regions. Vertically averaged volume flux vectors are displayed for the active layers (vectors less than < 2 m^2/s are masked) and the horizontal limits excluding the sluggish parts of the flow used for the "active G^2" estimation given in Fig. 11 are shown by the cyan lines, while local maxima of the layer Froude-numbers with major contribution to "active G^2" estimation are labeled across sections of the computational grid (run 5)

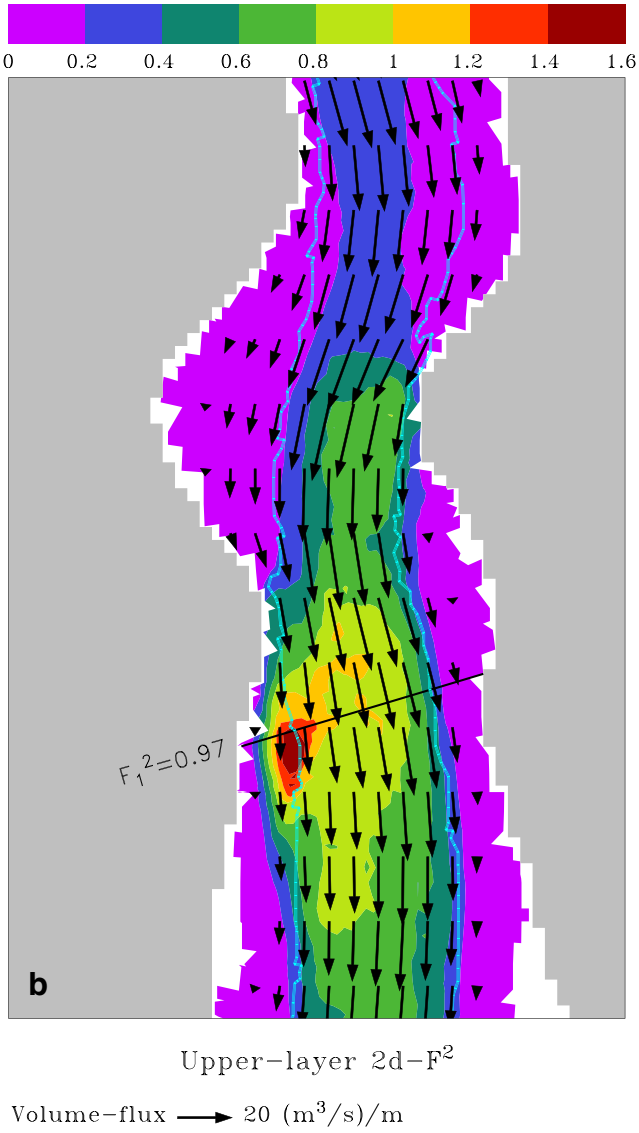

Fig. 12 (continued)

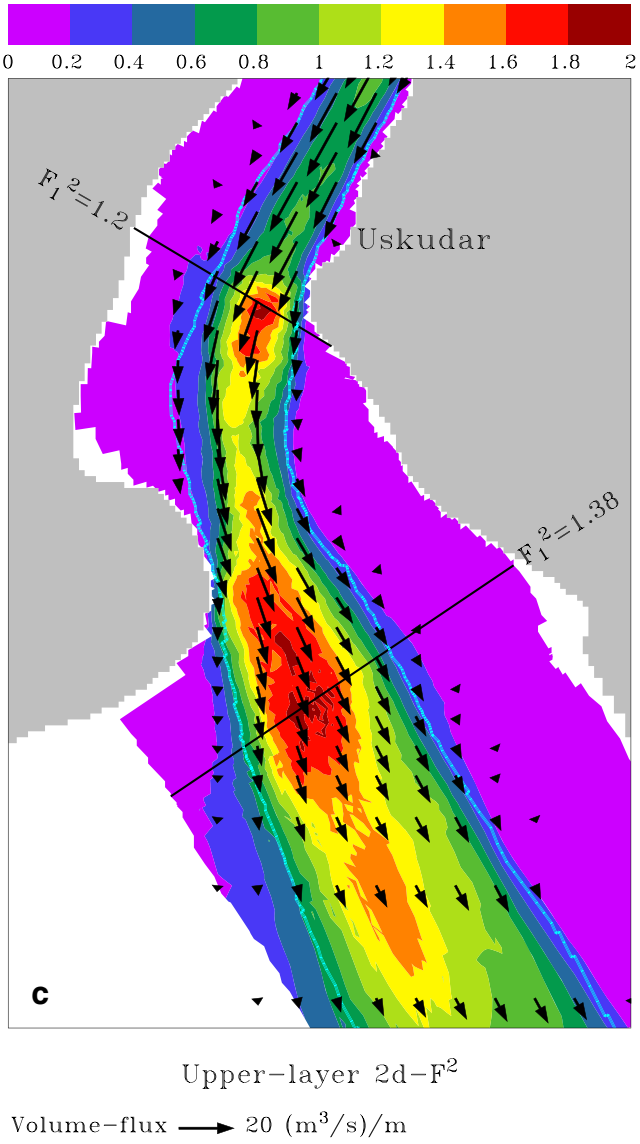

Fig. 12 (continued)

not exceeding the critical value, for example upon meeting the southern sill area. Further south, the upper-layer flow becomes asymmetrical, first leaning against the Asian shore as a narrow and fast current, becomes supercritical as it hits the protruding headland and its topographic extension into the strait at Üsküdar on the Asian side, before reaching the southern end of the strait. The flow then swings towards the European side against the Cape of Sarayburnu (Seraglio Point) and becomes supercritical once again as it exits from the abrupt opening into the Marmara Sea (Figs. 11 and 12c).

4.3.2 Three-layer approximation

Considering that an interfacial layer of variable density and velocity almost always exists in the Bosphorus, a three-layer approximation of the strait stratification would potentially provide a higher-order representation of the exchange flow characteristics. The three-layer criteria of hydraulic control has been developed by Smeed (2000) and Pratt (2008), while the latter author extended it to an N-layer system with Froude-number parametrization. Further details for the three-layer special case were given by Sannino et al. (2009) to demonstrate hydraulic criticality of the numerical solutions of the Gibraltar model. Since the degree-of-freedom of the system is increased to two internal modes in this case, an increased number of possible states exist in the three-layer system: (i) both modes supercritical, (ii) one of the modes supercritical while the other mode is subcritical, and (iii) both modes subcritical.

Further details of the three-layer Froude-number criteria defining the state of the flow is given in Section

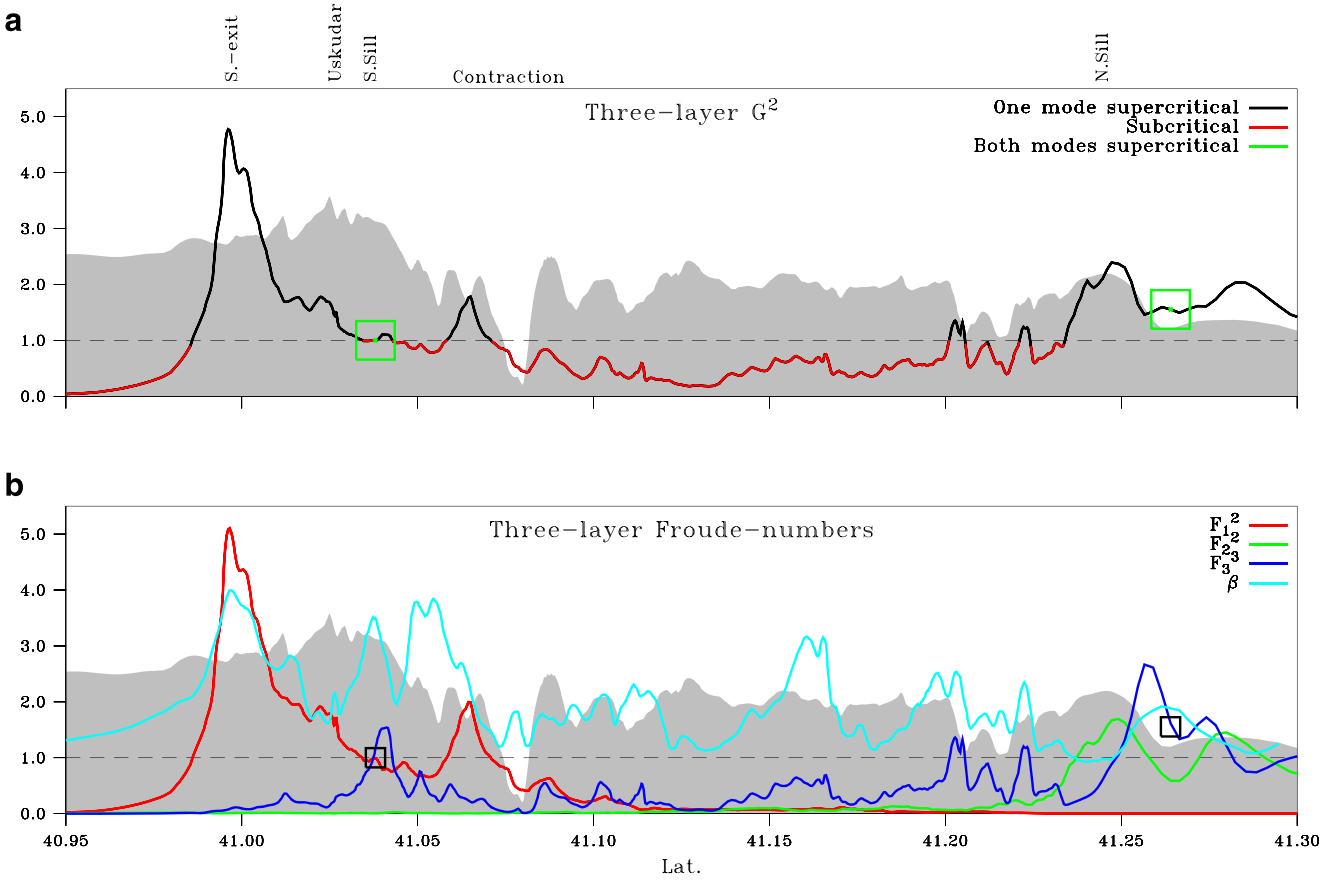

Fig. 13 (**a**) Three-layer composite Froude-number variation along the strait (run 5) showing the states of the flow based on the criteria of Sannino et al. (2009): subcritical (*red*), one mode supercritical (*black*) or both modes supercritical (*green*), (**b**) Froude-numbers F_i^2 for the layers $i = 1, 2, 3$ from top to bottom, and the parameter $\beta = [w_2(1-r)]/[w_3 r]$ (*cyan*), where $r = (\rho_2 - \rho_1) / (\rho_3 - \rho_1)$ is a density ratio and $w_{2,3}$ are the widths of the overlying interfaces. The bottom topography is shown by the gray background. Locations where both modes are found to be supercritical are marked by small squares

2b of Sannino et al. (2009). The three-layer composite Froude-number variation along the Bosphorus (run 5) is demonstrated in Fig. 13a assigning the three possible states to segments along the strait, based on criteria described above. As in the case of the two-layer calculation, the transverse variations are taken into account, although the vertical velocity shear corrections and the exclusion of the sluggish parts of flow used in the last section are not considered for the present estimates. The three-layer decomposition is performed by describing an interfacial-layer limited by the depths where a 12.5 % change in salinity occurs relative to the surface and the bottom values.

Evaluations based on the three-layer approximation for the composite densimetric Froude-number produce essentially similar results with the two-layer case: the flow state is almost completely subcritical between the contraction and the north sill, except for the region near the north end of the strait where sharp changes in topography and width influence to increase the lower-layer velocity (as indicated in Fig. 8 and also noted by Gregg and Özsoy (2002)). Outside of this region, we see that the flow is generally supercritical with respect to at least one mode with three distinctive composite Froude-number peaks at the south exit, contraction and at the north sill. Existence of both mode supercritical states between the south sill and the contraction and at the lee side of the north sill (marked by small squares in Fig. 13a) suggests a maximal exchange regime to exist, specific to the Bosphorus geometry and stratification. The individual contributions of the layer Froude-numbers F_i^2 and the parameter β characterizing a geometry/density ratio are shown in Fig. 13b, demonstrating the dominating role of the upper and lower layers respectively in the south and north Bosphorus, with a balanced mix of different factors leading to single- or multiple-mode critical transitions.

In the southern part of the strait, south the contraction, the flow reaches a single-mode supercritical state, falls back to subcritical state by dissipation, and once again reforms first briefly to reach a supercritical state for both modes, then continues with a singe-mode supercritical state reaching

a climax of single-mode supercritical state at the south-exit. Transition to the subcritical state follows rapidly, just after the south-exit, where the surface jet dissipates energy and spreads into the Marmara Sea. Despite reformations and fall-backs, a marginally critical state with the Froude-number close to unity is evident between the contraction and the south-exit, with supercritical states dominating and becoming supercritical at a control section involving both modes.

The flow is always supercritical at least with respect to one mode as soon as the lower-layer reaches and overflows the north sill, followed by a region where it becomes supercritical involving both modes, later dropping to a single mode. At the lee side of the north sill, the flow is always supercritical at least with respect to one mode, but as in the case of two-layer approximation, reformation of the flow after passing through the controls on the lee side of the north sill is again evident.

5 Discussion and conclusions

The TSS, being a transitional environment experiencing multiple stresses due to population and industrial pressures, is a fragile environment unprotected against mounting threats to its ecosystem. The TSS is a buffer between two highly contrasting basins allowing the exchange of water and materials influencing both ecosystems. Yet, the Marmara Sea has its own biochemical cycle that responds to inputs from neighboring seas and influences them.

The essential characteristic of the TSS is its complexity, while the Bosphorus Strait is the most significant element in the chain, determining the response of the entire coupled system. Observations suggest that the Bosphorus serves as the most restrictive element of the TSS connecting large marine basins through a unique regime of hydraulic controls in a stratified turbulent environment. Therefore, the Bosphorus Strait plays a major role in the series of complex multi-scale interactions and transformations both within the TSS and the adjacent seas.

Two different versions of the model have been used for the Bosphorus: (i) an idealized version with simple geometry designed to study the behavior of the Bosphorus Strait in response to the physical environment and (ii) a realistic geometry version with full topography to study the response of the Bosphorus Strait to realistic forcing. The study with the idealized model covered sensitivity tests (not completely covered in this paper) on the effects of the boundary and initial conditions, stratification and water budgets (inflow/outflows) in adjacent reservoirs, internal processes such as hydraulic controls and their influence on mixing. Steady-state solutions were always sought and achieved under the tested conditions, including cases of stratified boundary conditions where internal oscillations were damped to reach steady solutions.

The demonstration of the existence of hydraulic controls in the model required layers to be numerically identified in the model results for two- and three-layer approximations. Furthermore, accounting for velocity shears in the lateral (at the contraction and south-exit) and vertical (at the sill) directions of the flow was not straightforward to establish in the complex flow domain. The theoretical anticipation of hydraulic controls was tested under different settings, and in most cases, the results pointed to the existence of maximal-exchange, made possible by the existence of at least two hydraulic control sections where a critical transition occurred. For those cases of maximal-exchange, the layer fluxes were uniquely determined for a given net flux, under a certain range of the reservoir conditions excluding cases with drowned hydraulic controls.

The difference between the maximal-exchange and the drowned solutions presented under the idealized channel approximation demonstrated the need for precise representation of the Bosphorus Strait within a larger-scale model of the entire TSS accounting for the interaction between the Bosphorus Strait and the adjacent seas. An accurate representation of the strait geometry and topography determining the strait response is the most essential element needed in these implementations. Larger-scale models not sufficiently resolving the fine-scale topography and the internal dynamics of the straits would fail to accurately represent multi-scale, two-way coupling between the Black Sea and Marmara Sea and to capture the essential dynamical elements of the exchange.

In the realistic case, with either uniform or stratified boundary conditions, the results showed great agreement with the observed flow features and dynamical (e.g., sea level) response of the real Bosphorus. The flow field with many well-known meanders and recirculation areas and turbulent boils that are amongst the basic features evident to the casual observer as well as the experienced oceanographer are revealed in the model results, including similar features in the exit regions connecting the strait to the adjacent seas. Many observed features including the interface depth changes at hydraulic controls, the jet-like buoyant or negatively buoyant outflows into adjacent seas are successfully reproduced in the model.

One of the basic discrepancies between the steady-state model results and observations was found in the thickness of the interfacial-layer, which happened to be larger than what is observed; this difference was eventually minimized to be at the same level by tuning of the model parameters and could be further improved by increasing the model resolution and proper parametrization of mixing. Sensitivity tests (not given here) suggest the possibility

to run the model with zero horizontal diffusivity/viscosity, however, at the expense of very noisy results containing overshoots/undershoots in tracer fields and decreased numerical stability. With increased eddy resolving capability, increased number of vertical levels and decreased time step with some computational cost, or with improved parametrization of turbulence in strongly stratified conditions, it could be possible to improve model realism especially with respect to interface thickness.

In the case of uniform boundary conditions at the reservoirs, the results obtained inside the strait seem to be very robust to changes in reservoir density, with undetectable changes in the property distributions in the strait. One of the key findings was the separate paths followed by the centers of the upper- and lower-layer mean currents due to the meandering in the upper-layer and confinement to topography in the lower-layer. The two-layer definition is greatly depreciated in the southern Bosphorus past the contraction, where continuous shear velocity profiles are developed as the shear is increased in the whole depth of the top and interfacial layers.

The introduction of non-uniform boundary conditions had great impact in consequence to the intrusion of Black Sea water masses into the strait, the CIL making contact with the interface, changing the density and turbulence properties of the flow, in general making the interface less stable to turbulent fluctuations. At the same time, in response to the stratification change in the reservoirs, sea-level difference between basins and the layer fluxes and hence shear is decreased, and the interface thickness is increased. With the layer velocities also decreased, turbulence is decreased in the layers.

Hydraulic controls are easier to show at the north sill and the south-exit than the contraction with the use of the criteria based on the composite densimetric Froude-number, although it is difficult to do so with the plain criteria based on uniform two-layer approximation. It is only by taking into account the shear effects that the criteria can be updated with appropriate corrections and hydraulic controls can be established in the two-layer approximation. In the case of the realistic Bosphorus model with stratified boundary conditions, a higher-order specification with three-layers better validates hydraulic controls south of the contraction with phases of reformation and dissipation reaching the exit control, and in the same way, past the northern sill. Based on these results, it can be safely claimed that some form of complicated maximal-exchange regime, foreseen by the combined analysis of the sill-contraction couple in the literature appears to be valid in the Bosphorus.

The present study establishes the critical and leading role of the Bosphorus in controlling the exchange flows of the TSS and the resultant mixing between the exchanged water masses. In addition, the ultimate need to study the greater TSS domain, expounding upon the primary role of the Bosphorus has been clearly established. In companion papers (Sannino et al. 2016; Gürses et al. 2016) and in future publications based on collaborative research, we will continue exploring details that deserve further great attention.

Acknowledgments This study benefited from various independent observational studies carried out over the last 30 years at the IMS-METU, and research projects sponsored by the Turkish Scientific and Technical Research Council (TÜBİTAK), the FP7 European project SESAME, and past work carried out for the Water and Sewerage Administration of the Municipality of İstanbul (İSKİ), and the Defense Research Center of the İstanbul Technical University Foundation (İTÜV/SAM).

References

Armi L (1986) The hydraulics of two flowing layers with different densities. J Fluid Mech 163:27–58

Çetin N (1999) Analysis of the exchange flow through the Bosphorus Strait. Master's thesis Middle East Technical University. Institute of Marine Sciences, Turkey

Di Iorio D, Akal T, Guerrini P, Yüce H, Gezgin E (1999) Oceanographic measurements of the west Black Sea: June 15 to july 5, 1996. Tech. rep., Saclant Undersea Research Centre SR-305

Dorrell RM, Peakall J, Sumner EJ, Parsons DR, Darby SE, Wynn RB, Özsoy E, Tezcan D (2016) Flow dynamics and mixing processes in hydraulic jump arrays: implications for channel-lobe transition zones. Mar. Geol. doi:10.1016/j.margeo.2016.09.009

Farmer DM, Armi L (1986) Maximal two-layer exchange over a sill and through the combination of a sill and contraction with barotropic flow. J Fluid Mech 164:53–76

Filippi D LG, Iovenitti L, Akyarlı A (1986) Current analysis in the Marmara-Bosphorus Junction. 1st AIOM (Assoclazione di Ingegneria Offshore e Marina) Congress, Venice

Garrett C, Gerdes F (2003) Hydraulic control of homogeneous shear flows. J Fluid Mech 475:163–172

Gökaşan E, Tur H, Ecevitoğlu B, Görüm T, Türker A, Tok B, Çağlak F, Birkan H, Şimşek M (2005) Evidence and implications of massive erosion along the strait of istanbul (Bosphorus). Geo-Mar Lett 25(5):324-342

Gregg MC, Özsoy E (1999) Mixing on the Black Sea shelf north of the Bosphorus. Geophys Res Lett 26(13):1869–1872

Gregg MC, Özsoy E (2002) Flow, water mass changes, and hydraulics in the Bosphorus. J Geophys Res Oceans 107(C3):2–1–2–23

Gregg MC, Özsoy E, Latif MA (1999) Quasi-steady exchange flow in the Bosphorus. Geophys Res Lett 26(1):83–86

Gürses Ö, Aydoğdu A, Pinardi N, Özsoy E (2016) A Finite Element Modeling Study of the Turkish Straits System. In: Özsoy E, et al (eds) The Sea of Marmara - Marine Biodiversity, Fisheries, Conservation and Governance, Turkish Marine Research Foundation (TÜDAV)

Haidvogel DB, Arango HG, Hedström K, Beckmann A, Malanotte-Rizzoli P, Shchepetkin AF (2000) Model evaluation experiments in the North Atlantic basin: simulations in nonlinear terrain-following coordinates. Dyn Atmos Oceans 32(3-4):239–281

Hedström KS (1997) Draft user's manual for an s-coordinate primitive equation ocean circulation model (scrum) version 3.0. Institute of Marine and Coastal Sciences, Rutgers University

Ilıcak M, Özgökmen TM, Özsoy E, Fischer PF (2009) Non-hydrostatic modeling of exchange flows across complex geometries. Ocean Model 29(3):159–175

Jarosz E, Teague WJ, Book JW, Beşiktepe Ş (2011a) Observed volume fluxes in the Bosphorus Strait. Geophys Res Lett 38(21)

Jarosz E, Teague WJ, Book JW, Beşiktepe Ş (2011b) On flow variability in the Bosphorus Strait. J Geophys Res Oceans 116(C8)

Latif MA, Özsoy E, Oguz T, Ünlüata Ü (1991) Observations of the Mediterranean inflow into the Black Sea. Deep Sea Research Part A Oceanographic Research Papers 38(2(0)):S711–S723

Marsigli LF (1681) Osservazioni Intorno al Bosforo Tracio overo Canale di Constantinopoli Rappresentate in Lettera alla Sacra Real Maest Cristina Regina di Svezia da Luigi Ferdinando Marsigli. Nicol Angelo Tinassi, Roma

Oğuz T (2005) Hydraulic adjustments of the Bosphorus exchange flow. Geophys Res Lett 32(6)

Oğuz T, Sur HI (1989) A 2-layer model of water exchange through the Dardanelles Strait. Oceanol Acta 12(1):23–31

Oğuz T, Özsoy E, Latif MA, Sur HI, Ünlüata Ü (1990) Modeling of hydraulically controlled exchange flow in the Bosphorus Strait. J Phys Oceanogr 20(7):945–965

Özsoy E, Ünlüata Ü (1997) Oceanography of the black sea: a review of some recent results. Earth Sci Rev 42(4):231–272

Özsoy E, Ünlüata Ü (1998) The black sea. The Sea: The Global Coastal Ocean: regional studies and syntheses 11:889914

Özsoy E, Latif MA, Tuğrul S, Ünlüata Ü (1995) Exchanges with the Mediterranean, fluxes, and boundary mixing processes in the Black Sea, Bulletin de l'Institut Océanographique

Özsoy E, Latif MA, Sur HI, Goryachkin Y (1996) A review of the exchange flow regime and mixing in the Bosphorus Strait. Bulletin de l'Institut océanographique Monaco, Numera Special-

Özsoy E, Latif MA, Beşiktepe Ş, Çetin N, Gregg MC, Belokopytov V, Goryachkin Y, Diaconu V (1998) The Bosphorus Strait: exchange fluxes, currents and sea-level changes. NATO Science Series 2 Environmental Security 47(2):1–28

Özsoy E, Iorio DD, Gregg MC, Backhaus JO (2001) Mixing in the Bosphorus Strait and the Black Sea continental shelf: observations and a model of the dense water outflow. J Mar Syst 31(1-3):99–135

Özsoy E, Sözer A, Gündüz M, Yücel A, Yağcı B, Mert I, Yıldız H, Simav M, Elge M (2009) Meteorology and oceanography network of excellence (MOMA) observation and forecast systems. In: USMOS 09, National Defense Appications Modelling and Simulation Conference, Ankara

Pawlak G, Armi L (1997) Hydraulics of two-layer arrested wedge flows. J Hydraul Res 35(5):603–618

Pratt LJ (1986) Hydraulic control of sill flow with bottom friction. J Phys Oceanogr 16(11):1970–1980

Pratt LJ (2008) Critical conditions and composite Froude numbers for layered flow with transverse variations in velocity. J Fluid Mech 605:281–291

Pratt LJ, Johns W, Murray SP, Katsumata K (1999) Hydraulic interpretation of direct velocity measurements in the Bab al Mandab. J Phys Oceanogr 29(11):2769–2784

Sannino G, Pratt L, Carillo A (2009) Hydraulic criticality of the exchange flow through the Strait of Gibraltar. J Phys Oceanogr 39(11):2779–2799

Sannino G, Sözer A, Özsoy E (2016) A high-resolution modeling study of the Turkish Straits System, manuscript submitted for publication

Shchepetkin AF, McWilliams JC (2005) The regional oceanic modeling system (roms): a split-explicit, free-surface, topography-following-coordinate oceanic model. Ocean Model 9(4):347–404

Smagorinsky J (1963) General circulation experiments with the primitive equations: i. the basic experiment. Mon Weather Rev 91(3):99–164

Smeed DA (2000) Hydraulic control of three-layer exchange flows: application to the Bab al Mandab. J Phys Oceanogr 30(10):2574–2588

Sözer A, Özsoy E (2002) A three-dimensional model of Bosphorus Strait dynamics. In: The 2nd Meeting on the Physical Oceanography of Sea Straits, Villefranche, pp 207–210

Sözer A (2013) Numerical Modeling of the Bosphorus Exchange Flow Dynamics, Ph.D. thesis, Institute of Marine Sciences, Middle East Technical University Erdemli, Mersin, Turkey

Stashchuk N, Hutter K (2001) Modelling of water exchange through the Strait of the Dardanelles. Cont Shelf Res 21(13-14):1361–1382

Tolmazin DM (1967) Steady model of the water motion in stratified straits. In: Oceanographic studies of the black sea. Naukova Dumka, Kiev, pp 18–34

Tolmazin D (1985) Changing coastal oceanography of the Black Sea ii: Mediterranean effluent. Prog Oceanogr 15(4):277–316

Ünlüata Ü, Oğuz T, Latif M, Özsoy E (1990) On the physical oceanography of the Turkish Straits. In: Pratt LJ (ed) The physical oceanography of sea straits, NATO ASI series, vol 318. Springer, Netherlands, pp 25–60

Warner JC, Sherwood CR, Arango HG, Signell RP (2005) Performance of four turbulence closure models implemented using a generic length scale method. Ocean Model 8(1-2):81–113

Winters KB, Seim HE (2000) The role of dissipation and mixing in exchange flow through a contracting channel. J Fluid Mech:407